第 14 回
核燃焼プラズマ
統合コード研究会

14th Burning Plasma Simulation Initiative (BPSI) Meeting

日時：2016 年 12 月 7 日(水)－8 日(木)
場所：九州大学筑紫キャンパス
応用力学研究所 2 階大会議室

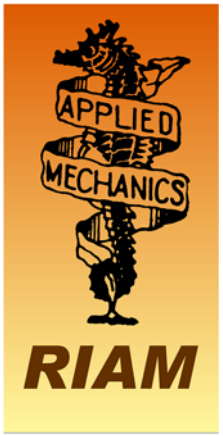

第 14 回核燃焼プラズマ統合コード研究会

14th Burning Plasma Simulation Initiative (BPSI) Meeting

(Ver.2)

日時：2016 年 12 月 7 日(水)－8 日(木)
場所：九州大学筑紫キャンパス　応用力学研究所 2 階大会議室

(18 min talk+7 min discuss or 10 min talk+5 min discuss)

12 月 7 日(水)

9:00 – 12:45　核融合エネルギーフォーラムサブクラスター会合

12:45 – 13:45　昼休み

13:45 – 13:55　はじめに　　村上 (京大)
(座長：村上)
13:55 – 14:20　講演 1-1　　藤田 (名大)
Analysis of axisymmetric equilibrium including magnetic field generated by energetic particles
14:20 – 14:45　講演 1-2　　本多 (量研機構)
Predictions of toroidal rotation and torque sources arising in non-axisymmetric perturbed magnetic fields in tokamaks
14:45 – 15:10　講演 1-3　　福山 (京大)
Status of integrated modeling activity for ITER
15:10 – 15:35　講演 1-4　　林 (量研機構)
Integrated modeling of JT-60SA high-beta steady-state scenario

15:35 – 15:50　休憩

(座長：藤田)
15:50 – 16:15　講演 1-5　　T. S. Hahm (Seoul Univ.)
Role of trapped electron dynamics in ITB formation
16:15 – 16:40　講演 1-6　　沼波 (核融合研)
Turbulent transport of multi-ion-species plasmas in helical systems
16:40 – 17:05　講演 1-7　　糟谷 (九大)
Turbulence diagnostic simulation for comparison with experiments
17:05 – 17:30　講演 1-8　　奴賀 (核融合研)
Fokker-Planck simulations of runaway electron generation in tokamak disruption

17:30　散会

19:00 – 21:00　懇親会（馳走 やまとや 博多駅東店にて）

12 月 8 日(木)

9:00 –　9:05　事務連絡
(座長：登田)
9:05 –　9:30　講演 2-1　　佐々木（九大）
Status and future plans of turbulence simulation on linear plasmas
9:30 –　9:55　講演 2-2　　小菅（九大）
Cross scale energy transfer in parallel flow shear driven turbulence
9:55 – 10:10　講演 2-3　　松井（九大）
Nonlinear simulation on profile formation with drift-wave instability in linear devices
10:10 – 10:25　講演 2-4　　阿部（九大）
Turbulence simulation of structural formation considering neutral particle profiles in linear devices

10:25 – 10:40　休憩

(座長：福山)
10:40 – 11:05　講演 2-5　　滝塚（阪大）
Kinetic simulation for edge plasma and detached divertor
11:05 – 11:30　講演 2-6　　東郷（筑波大）
Research on behavior of divertor particle flux with a one-dimensional numerical model and an analytical one
11:30 – 11:55　講演 2-7　　大澤（九大）
Vacancy cluster growth in tungsten induced by hydrogen

11:55 – 13:00　昼休み

(座長：糟谷)
13:00 – 13:25　講演 3-1　　矢木（量研機構）
Simulation study on internal transport barrier formation using gryofluid model
13:25 – 13:50　講演 3-2　　瀬戸（量研機構）
Linear analysis of non-ideal ballooning mode instability with real electron inertia

13:50 – 14:05　講演 3-3　　池田（京大）
PIC simulation of EC wave propagation and absorption in plasmas
14:05 – 14:20　講演 3-4　　永井（京大）
Start-up simulation of burning plasma by integrated modeling code TASK

14:20 – 14:35　休憩

(座長：矢木)
14:35 – 15:00　講演 3-5　　登田（核融合研）
Construction of reduced transport model by gyro- kinetic simulation with kinetic electrons in helical plasmas
15:00 – 15:25　講演 3-6　　村上（京大）
Prediction of neutron production in the deuterium experiment of LHD
15:25 – 15:40　講演 3-7　　前田（京大）
Heat and particle transport modeling of LHD plasma by integrated transport simulation
15:40 – 16:00　まとめ　　糟谷（九大）
16:00　散会

Analysis of axisymmetric equilibrium including magnetic field generated by energetic particles

T. Fujita

Graduate School of Engineering, Nagoya University
Furo-cho, Chikusa-ku, Nagoya 464-8603, Japan

A module for calculating an axisymmetric equilibrium considering current by fast particles with orbits shifted from the flux surface has been developed in the TOTAL code. Initial results indicate shift of the magnetic axis owing to the fast ion current.

1. Introduction

MHD equilibrium calculation is one of essential parts in an integrated transport code. In usual, the current density profile is evaluated in the form of the flux surface average of inner product of the current density $\boldsymbol{j}$ and the magnetic field $\boldsymbol{B}$, $\langle \boldsymbol{j} \cdot \boldsymbol{B} \rangle$ to be substituted to the Grad-Shafranov equation [1, 2].

$$\Delta^* \psi_p = \frac{\partial^2 \psi_p}{\partial R^2} - \frac{1}{R}\frac{\partial \psi_p}{\partial R} + \frac{\partial^2 \psi_p}{\partial Z^2} = -\mu_0 R j_{p\phi} \tag{1}$$

$$j_{p\phi}(R,\psi) = R\frac{dp}{d\psi} + \frac{F}{\mu_0 R}\frac{dF}{d\psi} = R\frac{dp}{d\psi}\left[1 - \frac{B_\phi^2}{\langle B^2 \rangle}\right] + \frac{\langle \boldsymbol{j} \cdot \boldsymbol{B} \rangle}{\langle B^2 \rangle} B_\phi \tag{2}$$

$$\langle \boldsymbol{j} \cdot \boldsymbol{B} \rangle = \langle \boldsymbol{j_{OH}} \cdot \boldsymbol{B} \rangle + \langle \boldsymbol{j_{BS}} \cdot \boldsymbol{B} \rangle + \langle \boldsymbol{j_{NB}} \cdot \boldsymbol{B} \rangle + \langle \boldsymbol{j_{RF}} \cdot \boldsymbol{B} \rangle + \cdots \tag{3}$$

where (R, ϕ, Z) is the cylindrical coordinate system, ψ_p is the ploidal flux function by the ϕ component of the plasma current density $j_{p\phi}$, $\psi = \psi_p + \psi_{ex}$ is the total ploidal flux function, ψ_{ex} is the poloidal flux function by the coil current, p is the total plasma pressure including the fast particle pressure and $F(\psi) = RB_\phi$. The $\boldsymbol{j_{OH}}$, $\boldsymbol{j_{BS}}$, $\boldsymbol{j_{NB}}$ and $\boldsymbol{j_{RF}}$ are the inductive current density, bootstrap current density, NB-driven current density and RF-driven current density, respectively.

This treatment seems to be incorrect for the current generated by energetic or fast particles whose orbits are not on the flux surfaces. In current hole plasmas, the shift of ion orbit from the flux surface is close to the order of the plasma minor radius [3]. In EC heated low-I_p plasmas, the electron orbit expands even outside of the last closed flux surface LCFS [4]. A self-consistent equilibrium including the fast particles was obtained before [5]. The model, however, focused on the runaway electrons and then the gyro-motion of energetic particles was not included.

In this article, we report on the formulation for finding an axisymmetric self-consistent equilibrium including the fast particle current and show some initial results.

2. Basic equations

Force balance equations in thermal or bulk plasma fluid and fast particle fluid are given by

$$\mathbf{0} = \boldsymbol{j_p} \times \boldsymbol{B} - \boldsymbol{\nabla} p_{th} \tag{4}$$

$$n_f (\boldsymbol{u_f} \cdot \nabla) m_f \boldsymbol{u_f} = \boldsymbol{j_f} \times \boldsymbol{B} - \boldsymbol{\nabla}_{\parallel} p_{\mathbf{f}\parallel} - \boldsymbol{\nabla}_{\perp} p_{\mathbf{f}\perp} \tag{5}$$

where $\boldsymbol{j_p}$ and p_{th} are the current density and the pressure of the thermal plasma fluid, $\boldsymbol{u_f}$ is the fast-particle fluid velocity and $p_{\mathbf{f}\parallel}$ and $p_{\mathbf{f}\perp}$ are components parallel and perpendicular to $\boldsymbol{B}$ of the pressure of the fast-particle fluid. In [4], monotonic energy beam without thermal pressure is assumed in the second equation. Then $\boldsymbol{u_f}$ can be replaced with the particle velocity $\boldsymbol{v_f}$ and eq. (5) becomes

$$n_f (\boldsymbol{v_f} \cdot \nabla) m_f \boldsymbol{v_f} = \boldsymbol{j_f} \times \boldsymbol{B}. \tag{6}$$

From eq. (6) a partial differential equation is obtained for U_f, the stream function of $\boldsymbol{v_f}$, which is solved simultaneously with the Grad-Shafranov equation.

In this study, we do not use the force balance in the fast particle fluid but trace the guiding-center orbit of fast particles. The slowing down and the pitch angle scattering by Coulomb collision are neglected. The guiding center orbit is calculated by using conservation of the ϕ component of canonical angular momentum P_ϕ given by eq. (7), where m and q_f are the mass and charge of the particle and $P_{\phi b}$ is the value of P_ϕ at the birth point of the particle. The toroidal component of the particle velocity v_ϕ is given by eq. (8), where $v_\parallel$ is the velocity parallel to $\boldsymbol{B}$, $v_{d\phi}$ is the ϕ component of the drift velocity $\boldsymbol{v_d}$ given by eq. (9). The $v_\parallel$ and $v_\perp$ (the gyro-motion velocity perpendicular to $\boldsymbol{B}$) are given by eqs. (10) and (11) by conservation of magnetic momentum and energy, where v is the magnitude of the particle velocity, B_b is the magntiude of $\boldsymbol{B}$ at the birth point and ξ is the ratio of $v_\parallel$ to v at the birth point.

$$P_\phi = mRv_\phi + q_f\psi = const. = P_{\phi b} \tag{7}$$

$$v_\phi = \frac{B_\phi}{B} v_\parallel + v_{d\phi} \tag{8}$$

$$\boldsymbol{v_d} = \frac{m}{q_f B}\left(v_\parallel^2 + \frac{v_\perp^2}{2}\right)\frac{\boldsymbol{B}\times\boldsymbol{\nabla}B}{B^2} \tag{9}$$

$$v_\parallel = v\sqrt{1 - \frac{B}{B_b}(1-\xi^2)} \tag{10}$$

$$v_\perp^2 = v^2\frac{B}{B_b}(1-\xi^2) \tag{11}$$

Note that ψ in eq. (7) contains the flux function by the fast particle current, ψ_f. Namely

$$\psi = \psi_p + \psi_f + \psi_{ex} \tag{12}$$

In this study it is assumed that no space electrostatic potential is generated by the fast particle even when their orbit expands outside LCFS. The potential would be canceled by existence of SOL plasma.

We fix the birth point of fast particles and trace the contour of P_ϕ. The rectangular grind in the RZ plane used for solving the Grad-Shafranov equation is used for tracing P_ϕ Once the P_ϕ contour is obtained, the distribution of the toroidal current by the fast particle is calculated along the orbit if the total number of particles is given. In this study, the total toroidal current by fast particles I_f is given instead of the total number of particles.

The Grad-Shafranov equation from eq. (4) is the same as eqs. (1) and (2), except that p is replaced with pth in eq. (2). In an integrated transport code the parallel current or $\langle \boldsymbol{j}\cdot\boldsymbol{B}\rangle$ is obtained by the transport module. In this study, the toroidal current density is given by the following equation instead of eq. (2).

$$j_{p\phi}(R,\psi) = R\frac{dp_{th}}{d\psi} + \frac{F}{\mu_0 R}\frac{dF}{d\psi} = \left[c_1\frac{R}{R_0} + (1-c_1)\frac{R_0}{R}\right]g(\tilde{\psi}) \tag{2'}$$

where c_1 is a constant, R_0 is the plasma major radius, $g(\tilde{\psi})$ is a function of $\tilde{\psi}$, and $\tilde{\psi}$ is the normalized poloidal flux function such that $\tilde{\psi} = 0$ at the magnetic axis and $\tilde{\psi} = 1$ on the LCFS. The function $g(\tilde{\psi})$ is determined such that the total thermal plasma current and the safety factor q at the axis become the given values.

A self-consistent solution of the Grad-Shafranov equation (1) and (2') and the orbit of fast particles (7) together with eq. (12) is obtained by iterating the following two steps. The first step is solving the Grad-Shafranov equation with the fixed fast particle current and then renewing ψ_p and ψ_{ex}. The second step is following the fast particle orbit with the given ψ and then renewing ψ_f. This process is iterated until ψ_p and ψ_f are converged. This procedure has been introduced into the initial equilibrium construction part in the integrated transport code TOTAL.

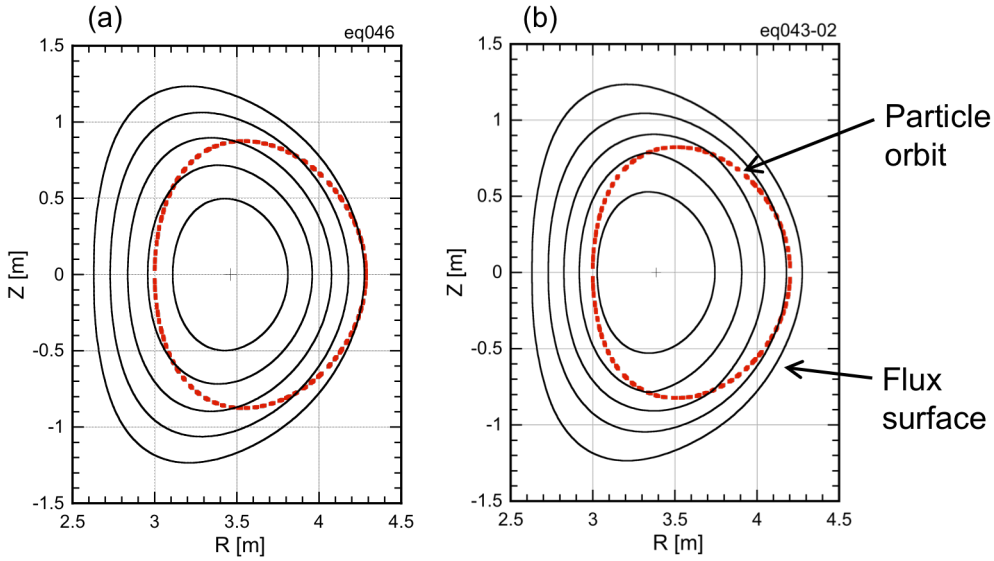

Fig. 1 Comparison of tokamak equilibria with and without fast ion current; (a) with bulk plasma current of 1 MA and no fast ion current (b) with bulk plasma current of 0.6 MA and fast ion current of 0.4 MA.

It is known that a return current by electrons is generated when a toroidal current is driven by fast ions circulating the torus. This effect is not yet included in the present analysis.

3. Results

The equilibrium including the fast particle current has been calculated as shown in Fig. 1. Here, the equilibrium without the fast particle current and that with the fast particle current are compared. The total toroidal current I_ϕ, sum of the bulk plasma current and the fast particle current is fixed to 1 MA. The shape of the LCFS is also fixed. As the fast particle, deuterium ions with 1 MeV energy and with $\xi = 1$ are generated at $R = 3$ m and $Z = 0$. The fast particle current I_f was 0 MA or negligibly small in Fig. 1 (a) and was 0.4 MA in Fig. 1 (b). It is found that the radial width of the fast ion orbit shown by dotted lines is smaller and the magnetic axis is shifted toward the high-field side in Fig. 1 (b) compared to Fig. 1 (a).

The q profiles are shown in Fig. 2. A nearly flat q profile with weak magnetic shear was employed. A localized negative shear region appears around $r/a = 0.5$ due to the localized fast ion current. Change in the q profile has possibility for affecting the shift of the magnetic axis shown in Fig. 1. It is needed to separate the effect of q profile change and that of current by fast particles with orbits shifted from the flux surface.

The convergence became slower with increasing I_f/I_ϕ. Tracing the particle orbit with fixed ψ would be one of the causes since it does not hold consistency between the particle orbit and ψ_f. Correction on this point would help to improve the convergence.

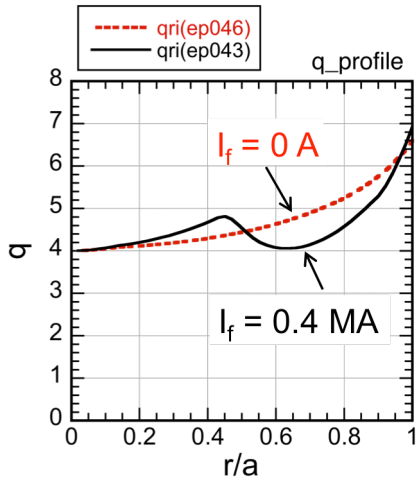

Fig. 2. The radial profile of safety factor q of equilibria shown in Fig. 1. The dotted line denotes the case without the fast ion current and the solid line denotes the case with the fast ion current.

Acknowledgments

This work was supported by JSPS KAKENHI Grand Number 25420895.

References

[1] S. Tokuda, et al., J. Phys. Soc. Japan **58**, 871 (1989).
[2] K. Tani, et al., J. Comp. Phys. **98**, 332 (1992).
[3] T. Fujita, Nucl. Fusion **50**, 113001 (2010).
[4] T. Maekawa et al. Nucl. Fusion **45**, 1439 (2005).
[5] Z. Yoshida, Nucl. Fusion **30**, 317 (1990).

Predictions of toroidal rotation and torque sources arising in non-axisymmetric perturbed magnetic fields in tokamaks

M. Honda, *S. Satake, *Y. Suzuki, K. Shinohara, M. Yoshida, §N. Aiba, J. Shiraishi, N. Hayashi, G. Matsunaga, *M. Nakata, §A. Matsuyama and S. Ide

National Institutes for Quantum and Radiological Science and Technology, Naka, Ibaraki 311-0193 Japan

**National Institute for Fusion Science, Toki, Gifu 509-5292 Japan*

*§National Institutes for Quantum and Radiological Science and Technology, Rokkasho, Aomori 039-3212 Ja*pan

Integrated modeling on toroidal rotation for developing operation scenarios

Toroidal rotation has attracted much attention in terms of not only the physics itself but also its influence on confinement and transport [1]. Accurate predictions of toroidal rotation are indispensable for those of plasma confinement. Recent advancement of the toroidal rotation modeling in the integrated suite of codes, TOPICS, with the 3D neoclassical transport solver, FORTEC-3D, and the 3D nonlinear equilibrium code, VMEC, enables us to perform analyses of toroidal momentum transport and the radial electric field E_r, and predictions of toroidal rotation with torque sources. The NTV stems from the non-axisymmetric perturbed magnetic fields in tokamaks and is an intrinsic torque source, which is expected to be a major momentum source in ITER and a DEMO reactor. Another intrinsic torque is the one due to the residual stress, which can spin up rotation from rest. The residual stress generally depends upon the temperature gradient [2]; hence, it is imperative to include the reliable residual stress model for developing high-performance operation scenarios with transport barriers.

The intrinsic torque due to perturbed magnetic fields

Thus far we have dealt with the n=18 symmetric non-resonant perturbed magnetic

field produced by the toroidal field (TF) coils and the ferromagnetic inserts (FIs) [3,4], where n is the toroidal mode number. However, ITER in reality have more complex perturbed magnetic field created by the heating and diagnostic ports and the TBMs. In particular, the TBMs give rise to large ripple amplitude of about 1% locally in the toroidal direction, which potentially enhances the loss of fast ions and transport of bulk ions. Each phenomenon is directly linked to the neutral beam injection (NBI) and NTV torques, respectively. The quantitative investigation of the impacts of the realistic perturbed magnetic fields on the estimate of the torque and toroidal rotation is of quite importance.

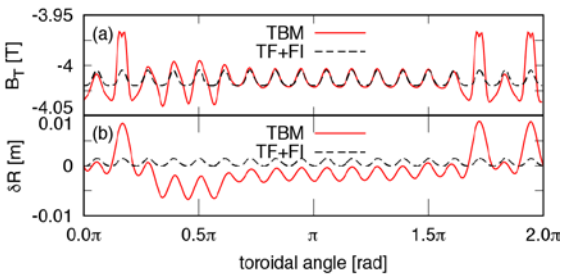

Figure 1: (a) Vacuum perturbed magnetic field at (R,Z)=(8.186,0.476) versus the toroidal angle. (b) Displacement of the LCFS of the equilibrium.

Effects of the non-axisymmetric perturbed magnetic fields on confinement of fast ions produced by NBIs and fusion reactions and on torque sources for the ITER 15MA DT L-mode scenario are investigated using the magnetic field produced by TF coils, FIs, ports and TBMs. The plasma response is considered in the equilibrium with the displacement of the last closed flux surface (LCFS) up to 1% of the minor radius. Figure 1 shows the δB amplitude and the plasma displacement δR, where one can see the existence of the three pairs of TBMs and the slight amplitude enhancement due to the ports. For reference, the 'TF+FI' case without effects of the TBMs and ports is also superimposed. The OFMC analysis shows that fast ions produced by 1MeV D-NBIs are never lost. Also, alpha particle confinement was investigated, indicating that 0.007% alphas merely ran away especially onto the divertor plates and no deterioration of alpha confinement due to TBMs was observed. These energetic particles are mostly passing ones and are insensitive to δB. These results are the beneficial findings that the TBMs and ports are unlikely to deteriorate fast-ion confinement and yield loss-related torques. In contrast, thermal ions are

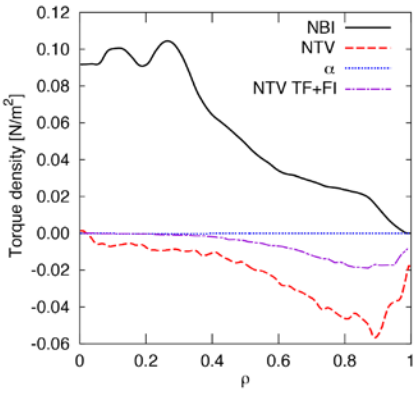

Figure 2: Profiles of torque density due to NBI, NTV and alphas.

significantly affected, as seen from the torque profiles in Fig. 2. Since the NTV increases towards the edge as the volume does, its torque becomes -23.5Nm, which is quite larger than that for the 'TF+FI' case, and is even comparable to the NBI torque of 30.3Nm. Applying the NTV decelerates core toroidal rotation from 180km/s to 145km/s. Simulations elucidate the essential importance of the NTV regarding rotation predictions in ITER.

The intrinsic torque due to the residual stress

The major unknown in the context of the rotation modeling is the residual stress. Calibrating the theory-based model [2] that can capture the experimental tendency is a practical way to attain rotation predictive capability for high-performance plasmas. A numerical factor C whose sign depends upon the dominant instability is added to the model and is examined with JT-60U data. For these shots possible torque sources have in advance been estimated, and the linear stability has been computed by the gyrokinetic code GKV. In Fig. 3, it is found that reproducibility of the carbon toroidal rotation $V_{\phi C}$ is to large extent improved, from dashed line to solid one, by the residual stress model with C=0.3 for this H-mode shot, where the ion temperature gradient (ITG) mode predominates in the edge region. It suggests a positive C, consistent with the C sign adopted here. The range of this factor is found to be $-1 \leq C \leq 1$ based on the several shots, a fact which can limit the range of predictions of toroidal rotation.

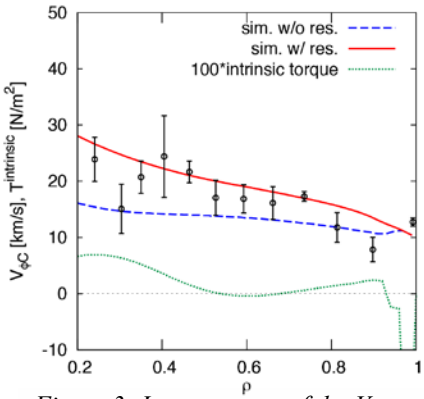

Figure 3: Improvement of the $V_{\phi C}$ reproducibility using the residual stress model with C=0.3.

References

[1] Mantica P et al., Phys. Rev. Lett. **107**, 135004 (2011).

[2] Kosuga Y et al., Phys. Plasmas **17**, 102313 (2010).

[3] Honda M et al., Nucl. Fusion **54**, 114005 (2014).

[4] Honda M et al., Nucl. Fusion **55**, 073033 (2015).

Integrated modeling of JT-60SA high-beta steady-state scenario

N. Hayashi, K. Hoshino, K. Shimizu, M. Honda, S. Ide

QST

The JT-60SA [1] mission is to contribute to early realization of fusion energy by supporting the exploitation of ITER and by complementing ITER in resolving key issues for DEMO reactors. Especially, JT-60SA explores the high-beta and steady-state operation regime to complement ITER. For the purpose, JT-60SA is equipped with flexibly applicable actuators of NB and EC. The scenario will use lower plasma current than the maximum one (5.5 MA), the plasma density needs to be lower and thus the reduction of divertor heat load is a critical issue. Impurity seeding to the divertor region can reduce the heat load below a preferable level of 10 MW/m^2, however, the accumulation of seeded impurity in the core may reduce the core confinement by enhancing the radiation and dilution.

In this paper, we predict the JT-60SA plasma by integrated modeling code TOPICS [2] which includes a divertor integrated code SONIC and a core impurity transport code IMPACT. For the prediction, we validate typical anomalous heat transport models, which are the major uncertainty in the prediction, for JT-60U and JET experiments with internal transport barriers in the Japan-EU collaborative activity. In the models, CDBM agrees with the experiments better than the other models, or underestimates temperatures. Thus, we consider that CDBM can be used for the conservative prediction. TOPICS with CDBM is used for the prediction without impurity seeding. A stationary state is obtained at the flat top phase of plasma current of I_p=2.3 MA with B_t=1.7 T. Various states with high-β_N (>3.5) and nearly full CD condition can be obtained by using various sets of actuators. By using the total power of 24 MW, a plasma with β_N=3.9 and nearly full CD condition is obtained. The scenario requires the low electron density at the separatrix ($n_{e,sep} < 1.7 \times 10^{19}$ m^{-3}), leading to the high heat load on divertor plates. SONIC simulations are carried out to find a solution satisfying the conditions by Ar seeding. With the

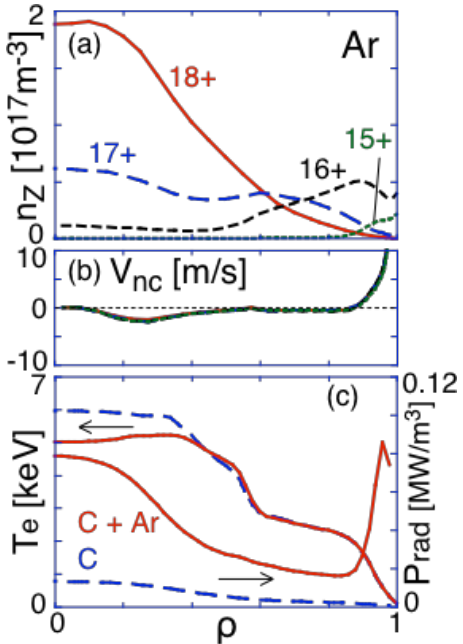

FIG. Profiles of (a) Ar densities with charge states from 15+ to 18+, (b) neoclassical convective velocities, (c) electron temperature and radiation power density in a case only with Carbon radiation (broken lines) and a case with seeded Ar (solid lines).

Ar puff amount of 0.17 Pa m^3/s, a solution with $n_{e,sep} = 1.6 \times 10^{19}$ m^{-3} and $q_{div,out} = 9.7$ MW/m^2 is obtained. TOPICS with IMPACT can clarify the accumulation of seeded Ar in the core and its effect on the plasma performance. Figure shows profiles of Ar densities, neoclassical convective velocities, electron temperature and radiation power density, where Ar densities at the edge evaluated by SONIC is used as boundary conditions in IMPACT to obtain the maximum accumulation. Considering the maximum accumulation, impurity anomalous diffusivities are set to the minimum level of neoclassical ones. The inward neoclassical pinch due to the bulk density gradient exists in the core and the outward convection due to the temperature gradient in the pedestal. This neoclassical convection results in the accumulation of Ar^{16-18+} in the core. The Ar radiation power increases by 3.8 MW and thus the temperature decreases in the core. The Ar accumulation reduces β_N to 3.6 so that the full CD condition is no longer satisfied. However, it can be recovered by adding the NB power to supplement the radiation increase.

Acknowledgments

This work was supported by a Grant-in-Aid for Scientific Research (C) (No 26420862) from the Japan Society for the Promotion of Science and was carried out using the HELIOS supercomputer at International Fusion Energy Research Centre, Aomori, Japan, under the Broader Approach collaboration between Euratom and Japan.

References

[1] JT-60SA Research Plan - Research Objectives and Strategy Version 3.3 2016, March, http://www.jt60sa.org/pdfs/JT-60SA_Res_Plan.pdf

[2] Hayashi N. *et al* 2010 *Phys. Plasmas* **17** 056112

実験との比較のための乱流計測シミュレーション

Turbulence diagnostic simulation for comparison with experiments

N. Kasuya and M. Nunami [1]
Research Institute for Applied Mechanics, Kyushu University, Kasuga, Fukuoka 816-8580, Japan
[1] National Institute for Fusion Science, Toki, Gifu 509-5292, Japan
E-mail: kasuya@riam.kyushu-u.ac.jp

Improvement of performance of helical plasmas is remarkable in these days. Consideration of the 3-dimensional (3-D) magnetic configurations is necessary for understanding their turbulent transport, but it is not simple to identify the observation region in the actual 3-D configurations, so numerical simulations can be used for the identification. Numerical simulations can be utilized for the synthetic analysis to simulate the experimental measurement [1,2] and the validation for the simulation result [3,4]. Many turbulence simulation codes have been developed for calculations in experimental magnetic configurations. For a helical plasma, using the GKV-X, which is a gyrokinetic Vlasov code with 3-D equilibrium, quantitative comparisons with experiments have been carried out [4]. Turbulence Diagnostic Simulator (TDS) [5] is a combination of turbulence codes, measurement modules and analysis routines, to carry out numerical experiments of plasma turbulence, which can be utilized as a platform of the data analysis. A numerical diagnostic to simulate an experimental measurement is carried out using gyrokinetic simulations of Ion-Temperature-Gradient (ITG) modes in the LHD configuration. The effect of line integration along the line of the sight (LS) is considered as in the Phase Contrast Imaging (PCI) measurement, and the spatial resolution for reconstruction of the local spectrum is evaluated.

Flux-tube simulations of ITG modes in the LHD configuration have been carried out with the GKV-X code [4]. The GKV-X is a nonlinear gyrokinetic Vlasov flux-tube code to perform turbulent transport simulations. The field aligned coordinate in the real space is used for calculations, and geometrical information of the flux surfaces is constructed by using VMEC code [6]. The adiabatic condition is used, so the electron density and the electrostatic potential is connected with the Boltzmann relation. Quantitative comparison of the thermal diffusivity coefficient has shown the good agreement with experiments [4], and other turbulent characteristics, such as a fluctuation spectrum, should be compared for validation.

We develop an analysis routine for the GKV-X data taking into account of a LS of experimental diagnostics, such as PCI. The PCI is used for the measurement of density fluctuation with high temporal and wavenumber k resolutions [7]. The signals are given as the integral of the density fluctuation along the LS. The GKV-X code uses the magnetic surface coordinate, so interpolation is necessary for evaluating the physical quantities in the real space. It must be noted that the obtained signal includes components perpendicular to the LS, so is usually combination of the radial and poloidal components, depending on the selection of the LS. To obtain k spectrum a finite region around the LS are picked out, and the quantities in it are evaluated with a finite spatial resolution, corresponding to the experimental diagnostic. The width and mesh size of the region determine the resolvable k range (resolution in the k space).

The GKV-X is the flux-tube code, so a set of the data is localized near one flux surface with a finite radial width. Figure 1 shows three sets of the density fluctuation data with different flux tubes (ρ = 0.43, 0.65, 0.83). The simulation parameters are written in Ref. [4]. Figure 1 also shows the LS for the numerical diagnostic, which views near the magnetic axis and is perpendicular to the mid-plane. The density patterns are calculated, and the k spectrum is obtained with Fourier transform with the Hanning window function. The line integration and temporal average gives the 2-D k spectrum from each flux-tube data. Here, the main components in the x and y directions are the toroidal and poloidal components, respectively. As the observation, all the density along the LS should be integrated, so every spectrum data is summed up with the weight of the mean density at the position. ITG modes have longer wavelengths in the direction of the magnetic field, so there are characteristic k_x - k_y relation in accordance with the magnetic field direction. Note that components with finite k along the LS become weak by the line integration, which reduces the contained components in the obtained signal.

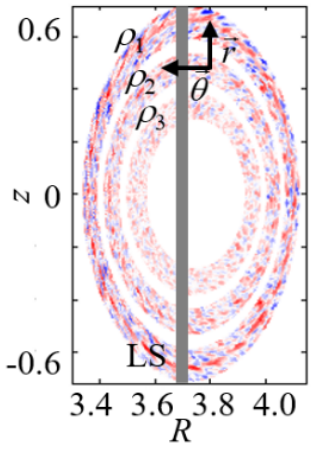

FIG 1. Fluctuation profiles from GKV-X gyrokinetic simulation at ρ = 0.43, 0.65, 0.83. The LS is also indicated by the gray bold line.

As the obtained signal from PCI is the line integrated one, so there is a problem to resolve the local values from the signal. The pitch angle of the magnetic field is used to help the identification [7]. The method to resolve the local spectrum from the integrated signal (2-D PCI) is applied using the simulation data. Assuming $k_{//} = 0$, the typical k direction can be set to be perpendicular to the magnetic field direction, which changes in accordance with the vertical position in helical plasmas. A vertical profile of the $|k_\perp|$ spectrum can be obtained by extracting the perpendicular components from the integrated signal (Fig. 2). The target fluctuations exist at the limited radial range, but the reconstructed profile spreads in the wider region. Larger part of the leakage comes from discreteness of the data with the finite spatial resolution. The discrete Fourier transform cannot avoid the leakage, so the resolution is limited to the mesh size in the k space. The variation of the magnetic field direction in the region to calculate the spectrum gives other cause for the errors, whose contribution is comparable to the former one. Broadened fluctuation spectrum in local positions is also one of the causes for the deterioration. For the decomposition using the magnetic shear, the mesh

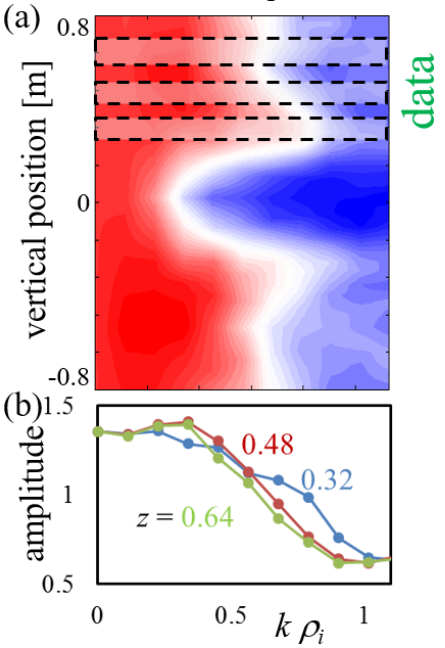

FIG 2. (a) Vertical profile of the k spectrum decomposed by using the magnetic shear method. (b) Spectra at z, where the fluctuation data exists, are also plotted.

is sparser with smaller k, so the spatial resolution is worse with smaller k: $\Delta z \sim 0.2$ at $k\rho_i = 0.1$, $\Delta z \sim 0.1$ at $k\rho_i = 0.4$ in the case at $z = 0.6$ in Fig. 2, where ρ_i is the ion Larmor radius. The local spectrum must be discussed with careful consideration of the spatial resolution.

The analysis routine can give a fluctuation pattern at an arbitrary position, and comparison between the local fluctuation and the decomposition of the integrated signal gives understanding of the observed signals. The ITG modes have a characteristic wavelength and frequency, and difference in the spectrum can be distinguished at different radial positions, considering the spatial resolution. The propagation direction can be also deduced from this spectrum. This is the rather simple case to observe the kθ components, but other LSs give combination of the k_r and k_θ components, which makes the spectrum complex for interpretation.

In this way, the numerical diagnostics have been carried out in the 3-D torus magnetic configurations. For the 2-D PCI, one way to improve the spatial resolution is to apply the other conversion method, such as the maximum entropy method [7]. Considering the rough spatial resolution, quantities distant enough from each other can be identical, so the diagnostics will be applied for evaluation of the up-down asymmetry and detection of long-range correlation in future. Variety of the numerical diagnostics from several view-points can give physical understanding and quantitative comparison of turbulent plasmas.

Acknowledgements
Authors acknowledge discussions with Prof. K. Itoh, Prof. S.-I. Itoh, Prof. S. Inagaki, Prof. K. Tanaka, Prof. K. Ida, Dr. S. Toda, and Mr. K. Kawadu. This work is supported by JSPS KAKENHI Grant Number JP24760703 and JP16K06938, by the collaboration program of NIFS (NIFS15KNST082, NIFS16KNXN323, NIFS13KOCT001) and of RIAM of Kyushu University.

References
[1] LIN, L., et al., Phys. Plasmas 16 (2009) 012502.
[2] HOLLAND, C. et al., Phys. Plasmas 16 (2009) 052301.
[3] RHODES, T.L., et al., Nucl. Fusion 51 (2011) 063022.
[4] NUNAMI, M., et al., Phys. Plasmas 19 (2012) 042504.
[5] KASUYA, N., et al., Plasma Fusion Res. 8 (2013) 2403070.
[6] SUZUKI, Y., *et al.*, Nucl. Fusion **46** (2006) L19.
[7] TANAKA, K., et al., Rev. Sci. Instrum. 79 (2008) 10E702.

Fokker-Planck simulations of runaway electron generation in tokamak disruption

H. NUGA[1], M. YAGI[2], A. FUKUYAMA[3]

[1]National Institute for Fusion Science
[2]National Institutes for Quantum and Radiological Science and Technology
[3]Department of Nuclear Engineering, Kyoto University

Introduction Disruption is one of the most serious events in tokamak discharges, since it induces huge electromagnetic force to the device and generates high-energy runaway electrons (REs) which may cause the damage of the plasma facing components[1]. Especially in large size tokamak, such as ITER, since there is a possibility that the RE current can reach to a few mega-amperes and cause intolerable heat load to the first wall, the damages should be avoided or suppressed. To avoid the disruption and related damages, the fast plasma shutdown by means of Massive Gas Injection (MGI) has been proposed and demonstrated in several devices. It is expected that the high electron density plasma achieved by MGI may reduce the RE generation owing to its high collisionality. MGI for mitigating disruption, however, tends to yield the shorter thermal quench duration and may enhance the primary RE generation rate through the so-called "hot-tail effect"[2, 3].

Aim of this paper is the investigation of the RE current generation in the MGI mitigating plasma including hot-tail (H-T) effect. To include the H-T effect, the primary RE generation rate is evaluated by the electron momentum distribution function obtained by using Fokker-Planck code TASK/FP. Evolutions of RE generation and induced electric field are calculated self-consistently. Additionally, the drop of the plasma temperature and the increase of the electron density and the effective charge owing to MGI are implemented simply.

Models In the present research, we use Fokker-Planck code TASK/FP to obtain the primary RE generation rate and the induced toroidal electric field self-consistently. The detailed expression of the models of the primary and secondary RE generation rates, the induced electric field, and the thermal quench are displayed in [4].

Additionally, the evolutions of electron and ions densities and the effective charge assuming MGI are modeled. Usually, noble gases, such as neon or argon, are used for MGI. In the low temperature plasma ($\sim$ tens of eV), however, most of impurity ions are not fully ionized. Since the issue of ionization state of impurities is also complex, to simplify our model, we introduce post-MGI effective charge $Z^f_{\rm eff}$ and virtual impurity ion species, which has no electron-bound state. They satisfy the following relations: $n^f_e = n^0_e + Z_i n^f_i, \quad Z^f_{\rm eff} = (n_D + Z_i^2 n^f_i)/n^f_e$, where superscript 0 and f denote pre- and post-MGI density or efffective charge, respectively. We assume that electron density evolves as follows:

$$n_e(\rho) = (n^f_e(\rho) - n^0_e(\rho))\frac{t}{\Delta t_{\rm MGI}} + n^0_e(\rho) \quad (t \le \Delta t_{\rm MGI}) \tag{1}$$

$$= n^f_e(\rho) \quad (\Delta t_{\rm MGI} \le t), \tag{2}$$

Figure 1: Plasma parameters

Radii	$R = 6.2$m, $a = 2.0$m, $b = 2.4$m
Initial current	15 MA
Initial temperature	$T_0(0) = 20$ keV, $T_0(1) = 2$ keV
Post-quench temp.	$T_f(0) = 10$ eV
Thermal quench time	$\tau_q = 1$ ms
MGI duration	$\Delta t_{\rm MGI} = 5$ms
Pre-quench density	
on axis	$n_e^0(0) = 1.0 \times 10^{20}$m^{-3}
on edge	$n_e^0(1) = 1.0 \times 10^{19}$m^{-3}
effective charge	$Z_{\rm eff}^0 = 1$, $Z_{\rm eff}^f = 3$
Ion species	Deuteron

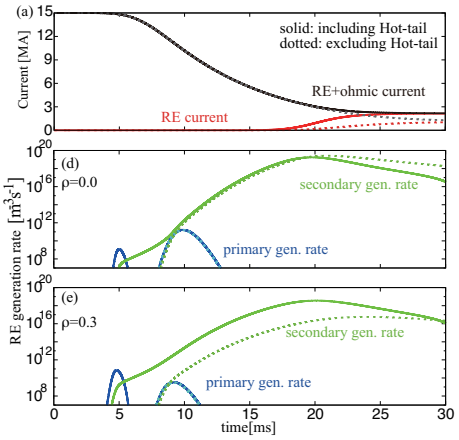

Figure 3: Evolutions of (a): Total and RE current, (b): primary and secondary RE generation rates on axis and (c) on $\rho = 0.3$.

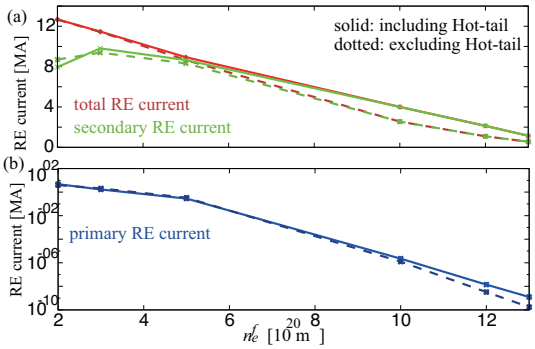

Figure 2: $n_e^f(0)$ dependence of the total, primary, and secondary RE current for $\tau_q = 1$ ms, $\Delta t_{\rm MGI} = 5$ms, and $Z_{\rm eff}^f = 3$.

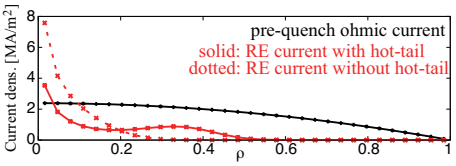

Figure 4: Current density profile for $n_e^f(0) = 12 \times 10^{20}$ m^{-3}.

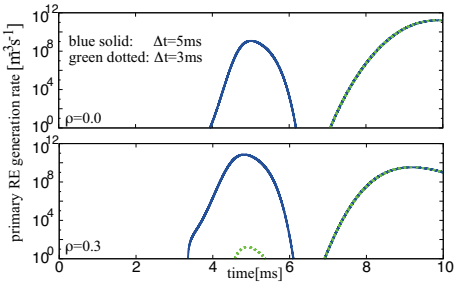

Figure 5: Primary RE generation rate on axis and $\rho = 0.3$ for $\Delta t_{\rm MGI} = 5$ ms and 3 ms.

where $\Delta t_{\rm MGI}$ is the duration in which the electron density increases. Here, impurity transport is omitted for simplicity.

Results In the following calculation, we chose parameters tabulated in Table 1.

Figure 2 shows the $n_e^f(0)$ dependence of the (a) total, secondary, and (b) primary RE current. It is found that the density increase achieves to suppress the RE generation as expected. In low density region ($n_e^f(0) = 2 \times 10^{20}$ m^{-3}), most of pre-quench ohmic current is converted into RE current (total RE current: $I_{\rm RE} = 12.7$ MA). The primary RE current excluding H-T effect is $I_{\rm prim} = 3.96$ MA and that including H-T effect increases to $I_{\rm prim} = 4.73$ MA.

Subsequently, we focus on high electron density case ($n_e^f(0) = 1.2 \times 10^{21}$ m^{-3}). Although the high electron density succeeds to suppress the RE generation, the presence of the H-T effect makes the total RE current twice in the region ($I_{\rm RE} = 1.09$ and 2.12 MA for excluding and including H-T effect cases). In this case, H-T effect enhances the primary RE current about four times ($I_{\rm prim} = 3.3$ mA to 14 mA), though the magnitude of the increment (~ 11 mA) is very small compared to total

RE current. This small increment of the primary RE current is multiplied by the avalanche effect to 1.03 MA and total RE current becomes twice. Figures 3 show the evolutions of (a) total and RE current, and (b) primary and secondary RE generation rates on axis and (c) $\rho = 0.3$. From fig. 3 (b) and (c), it is found that the H-T effect makes a additional peak of the primary RE generation rate ($t \sim 5$ ms). This is because, H-T electrons can be REs easily rather than bulk electrons even with the weak electric field due to the low collisionality. Owing to the presence of earlier seed REs, the secondary RE generation is also triggered earlier. On $\rho = 0.3$, since the primary RE generation rate at first additional peak ($t \sim 5$ ms) is sufficiently greater than that at subsequent peak, the secondary RE current density also becomes greater. Figure 4 shows the initial ohmic and RE current density profiles for $n_e^f(0) = 1.2 \times 10^{21}$ m^{-3} case. The RE current density profiles have a peak on axis rather than the initial profile. Furthermore, the H-T effect makes the peak lower and broadens the RE current profile.

This result shows that the presence of the first additional peak of ($t \sim 5$ ms) multiplies the total RE current. Since $\Delta t_{\mathrm{MGI}} = 5$ ms is chosen in this result, the RE generation from H-T electrons begins before the electron density reaches to post-MGI density n_e^f. Therefore, $\Delta t_{\mathrm{MGI}} = 3$ ms is chosen to investigate the behavior of the H-T RE peak.

Figure 5 shows the primary RE generation rate for $\Delta t_{\mathrm{MGI}} = 5$ ms and 3 ms cases. It is found that the faster increase of the electron density achieves to suppress the H-T RE generation ($t \sim 5$ ms) both on axis and $\rho = 0.3$. Consequently total RE current is also suppressed from 2.12MA ($\Delta t_{\mathrm{MGI}} = 5$ms) to 1.10 MA ($\Delta t_{\mathrm{MGI}} = 3$ms), which nearly equals to the result excluding H-T effect (1.09MA, $\Delta t_{\mathrm{MGI}} = 3$ms).

Summary The present simulation study makes clear that the H-T effect is important for the RE generation with short thermal quench even in high electron density plasma. We have confirmed that the RE generation is suppressed with the increase of the electron density. If the H-T effect is not considered, the RE generation is reduced to $\sim$ 1 MA in the high density region ($n_e^f(0) = 1.2 \times 10^{21}$ m^{-3}). On the other hand, if the H-T effect is included, the effect multiplies the primary RE current slightly ($\sim$ 10 mA) and, consequently, total RE current is doubled due to avalanche effect. This multiplication comes from the fact that H-T electrons can be REs earlier than bulk electrons owing to its low collisionality. If the electron density increases up insufficiently until the H-T RE generation starts, the H-T effect multiplies the primary RE current. Conversely, it is also confirmed that sufficiently fast increase of the electron density may suppress the H-T RE generation. Because of these reasons, the reliable estimation of the thermal quench, increase of the electron density, and impurity transport are inevitable.

[1] T.C. Hender *et al.*, Nuclear Fusion, **47**, S128 (2007)
[2] H. M. Smith and E. Verwichte, Phys. Plasmas, **15**, 072502, (2008).
[3] T. Fehér, *et. al.*, Plasma Phys. Control. Fusion, **53**, 035014, (2011).
[4] H. Nuga, *et at.*, Phys. Plasmas, **23**, 062506, (2016).

Status and future plans of turbulence simulation on linear plasmas

M. Sasaki[1, 2]

[1]Research Institute for Applied Mechanics, Kyushu University, Kasuga 816-8580, Japan
[2]Research Center for Plasma Turbulence, Kyushu University, Kasuga 816-8580, Japan

1 Introduction

Importance of the parallel flows has been recognized in magnetized plasmas. Intrinsic toroidal rotation in toroidal plasmas and the flows around cusp region of the earth's magnetic field [1, 2]. In the case when the shear of the parallel flow becomes large, the flow shear instability, which is called D'Angelo mode, occurs [3, 4]. In a linearly magnetized plasma device, PANTA, this shear flow instability was observed, and the density peaking by the D'Angelo mode was observed. The relation between the particle and momentum transport was investigated [5], and the spatial structure of the D'Angelo mode was identified [6]. In this way, the experimental studies have been developed. The turbulence simulation on the D'Angelo mode is required to accelarate the fundamental nonlinear processes of the shear flow instability.

2 Model

In this study, we develop a turbulence simulation code to simulate the D'Angelo mode. Based on the Numerical Linear Device (NLD) code [7], the ion parallel flow is included. The model is a reduced fluid model to calculate the time evolution of the density, electrostatic potential and the parallel ion flow. This mode is an extension of Hasegawa-Wakatani model with coupling of the ion parallel flow, which can simulate the resistive drift wave and the D'Angelo mode. The mean density and the ion parallel flow are introduced by giving the particle and parallel momentum sources, respectively.

3 Results

The bifurcation of the turbulence states between the drift wave dominant state and the D'Angelo mode dominant state by changing the strength of the density source with the shot-by-shot manner, where the parallel momentum source is kept constant. The mode spectrums in each turbulence state are shown in Fig. 1. The change between the two states is abrupt, which has not been observed in experiments. The drift wave dominant case is obtained in the case that the density source is large. The symmetry parallel mode spectrum is obtained in this case, which is consistent with the previous studies as in [7]. The drift waves forms the streamer in this case. When the density source is small and the density gradient becomes small, the D'Angelo mode is

excited by the parallel flow shear. In this case, the asymmetry of the parallel mode spectrum is obtained. The higher harmonics are excited and the nonlinear structure with $(m, n) = (0, n)$ was obtained. The spectrum asymmetry and the spatial structure of the eigenfunction are consistent with the theoretical prediction [4] and the experiments [6]. The roles of each turbulence on the density and the parallel flow are also studied by evaluating the density and parallel momentum flux. In the case of the drift wave dominant state, the density fluctuation flattens the density profile, and the parallel momentum flux is relatively weak due to the fact that the parallel mode spectrum is almost symmetry. In the D'Angelo mode dominant state, the fluctuation with the parallel mode spectrum asymmetry effectively drives the parallel momentum flux, which works to flatten the profile of the parallel flow. For the density flux, we obtain the inward particle flux, which steepens the density profile. These characteristics are found to be similar to the experiment [5].

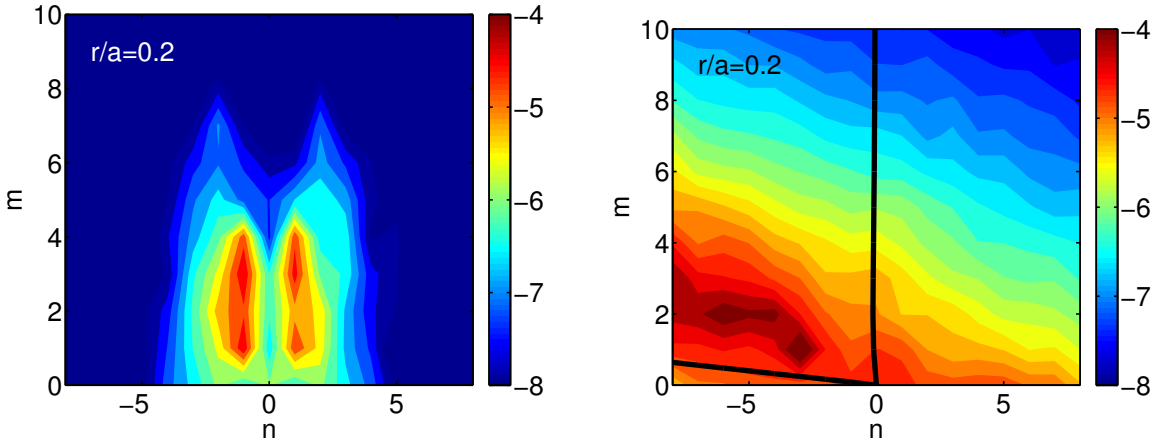

Fig. 1: Mode spectrums of the drift wave dominant state (left) and the D'Angelo mode dominant state (right). Here m and n are the azimuthal and parallel mode numbers, respectively. The spectrums are calculated from the potential fluctuations at $r/a = 0.2$.

References

[1] P. H. Diamond, et. al., Nucl. Fusion, **49**, 045002 (2009).

[2] H. Hasegawa, et. al., Nature, **430**, 755 (2004).

[3] N. D'Angelo, Phys. Fluids, **8**, 1748 (1965).

[4] Y. Kosuga, et. al., Plasma Fusion Res. **10**, 3401024 (2015).

[5] S. Inagaki, et. al., Scientific Reports, **6**, 22189 (2016).

[6] N. Dupertuis, et. al., Plasma Fusion Res. 12 1201008 (2017).

[7] N. Kasuya, et. al., Plasma Phys., **15**, 052302 (2008).

Cross scale energy transfer in parallel flow shear driven turbulence

Y. Kosuga[1,2]

[1] Research Institute for Applied Mechanics, Kyushu University, Fukuoka, Japan

[2] Research Center for Plasma Turbulence, Kyushu University, Fukuoka, Japan

Flows along the magnetic field (parallel flows, in short) are ubiquitous in space and laboratory plasmas. In particular, in fusion plasmas, parallel flows are observed in scrape off layer plasmas[1] and ITB plasmas[2]. In these regions, parallel flows with the Mach number close to unity are observed. These flows can be source of fluctuation, which impact transport processes in other channels. Indeed, coupled dynamics of parallel momentum transport and particle transport is observed on recent studies[3].

A key to understand the underlying dynamics is the interplay between drift wave turbulence and parallel flow shear driven turbulence. While previous studies reveal a basic feature of parallel flow shear driven mode, there nonlinear physics remains elusive. Once nonlinear coupling is invoked, cross-scale energy transfer comes into play. In this process, energy in the primary mode can be distributed to different scales, including larger scales. As a result, large scale structure, such as zonal flows[4,5] can be generated in parallel flow shear driven turbulence.

In addition to zonal flows, several other secondary structures can arise as a consequence of nonlinear interaction. In this work, we discuss generation of large scale convective cells in parallel flow shear driven turbulence. Nonlinear energy transfer among primary parallel flow shear driven mode and secondary convective cells is formulated. Performing closure calculation, we obtain the nonlinear growth rate of convective cells. As a limiting cases, we discuss the generation of i.) zonal flows, poloidally elongated cells and ii.) streamers, radially elongated cells. It is shown that both structures can be realized in parallel flow shear driven turbulence. Since two different structures are possible, a relevant question is which type of structure is formed. In other words, what is the selection rule of a structure in parallel flow shear driven turbulence? From deterministic point of view, we discuss that zonal flows are preferred. This is due to the fact that for cells with finite poloidal wave

number, sideband in parallel velocity fluctuation tends to prohibit the accumulation of energy in large scale. In a extreme case, we argue that while energy can be pumped into zonal flows, radially elongated cells with finite poloidal wave numbers do not gain energy and rather pump smaller scales. Relation to the observed high frequency component of parallel flow velocity fluctuation is discussed.

Stimulating discussion with Drs. S.-I. Itoh, K. Itoh, S. Inagaki, T. Kobayashi, P.H. Diamond, L. Wang, and Z. Guo is acknowledged. This work was supported by Grants-in-Aid for Scientific Research of JSPF of Japan (JP15H02155, JP15K17799), Kyushu University Interdisciplinary Programs in Education and Projects in Research Development (TT26705) and QR program (28315).

References

[1] X. Garbet, et al., Phys. Plasmas **6** 3955 (1999)

[2] X. Garbet, at al., Phys. Plasmas **9** 3893 (2002)

[3] S. Inagaki, et al., Sci. Rep. **6** 22189 (2013)

[4] P.H. Diamond, et al., Plasma Phys. Control. Fusion **47** R35 (2005)

[5] Y. Kosuga, et al., submitted to Phys. Plasmas (2016)

直線装置における分布形成に関するドリフト波不安定性の非線形シミュレーション

Nonlinear simulation on profile formation with drift-wave instability in linear devices

Y. Matsui [1], N. Kasuya [1,2], M. Sasaki [1,2], S. Abe [1], S. Inagaki [1,2] and M. Yagi [3]

[1] Interdisciplinary Graduate School of Engineering Science, Kyushu University, Kasuga, Fukuoka 816-8580, Japan

[2] Research Institute for Applied Mechanics, Kyushu University, Kasuga, Fukuoka 816-8580, Japan

[3] National Institute for Quantum and Radiological Science and Technology, Obuchi, Rokkasho, Aomori 039-3212, Japan

E-mail: matsui.yousuke@riam.kyushu-u.ac.jp

Turbulent structural formation is one of the keys for understanding transport phenomena in magnetized fusion plasmas. We have been carrying out the research of turbulent structural formation with resistive drift-wave instability in linear devices [1]. Numerical Linear Device (NLD) [2] is a numerical simulation code of resistive drift-wave turbulence in linear devices, and is used for quantitative predictions of experimental observations. In experiments in linear device PANTA, bifurcation between turbulent structures, as streamer [3] and solitary drift-wave [4], has been observed. In addition, a theory predicts the bifurcation of the position of the steep wave front of the solitary drift-wave [5]. In this research, stability and structural formation condition of resistive drift-wave turbulence are investigated by scaning of the plasma parameters using the NLD code to understand the parameter dependency and effect of the mean profile formation with turbulent structures.

A numerical simulation code has been developed for resistive drift wave in linear devices [2]. The plasma geometry is assumed to be a simple cylinder and the magnetic field has only the axial component with uniform intensity. According to the experiments in PANTA device, we focus on high-density and low-temperature plasmas in an argon discharge. Neutral particles also exist inside the plasma and its effect must be taken into account. The code is based on the three-field (density, electrostatic potential, and parallel velocity of electrons) reduced fluid equations, which consist of the continuity equation, the charge conservation equation, and the momentum conservation equation. The model is an extension of the Hasegawa-Wakatani model by taking neutral particle effects into account. The periodic boundary conditions are assumed in the azimuthal and axial directions, which allow the spectral expansion. We describe the drift wave by nonlinear simulations using parameters; electron temperature $T_e = 2$ [eV], plasma radius $a = 7$ [cm], length of the device $\lambda = 4$ [m]. Simulations are carried out with a time independent particle source. The density profile in plasma is formed self-consistently by balance of the particle supply, turbulence fluxes, and collisional transport. In the edge region, plasma particles are lost by the collisional transport. Focusing on basic nonlinear processes for turbulence caused by the density gradient, we do not consider the moment source induced by a particle source here. The modes that has azimuthal mode number $m = 0$ are linearly stable, but the nonlinear interaction of drift waves can drive these modes. Using these parameters, the time evolution of each mode is calculated by solving the set of equations.

Time evolutions of fluctuations are calculated with the fixed particle source term. Time evolution of the energy of each Fourier component of the density fluctuation is shown in Fig. (a). This is the case when the streamer is formed. The dominant modes, which are nonlinearly coupled to each other, have (m, n) = (2, 1) and (3, 1), where m and n are azimuthal and axial mode number, respectively. The density profile is flattened in the nonlinear evolution to make the modes less unstable, and only these two modes are unstable in the saturated state. The growth rate is evaluated by using the instantaneous background density and potential profiles. In this case, the effect of the potential formation is little. The growth rate dependencies on magnetic field B and collision frequency ν_{in} of (m, n) = (2, 1) mode and (3, 1) mode are calculated as in Fig. (b) and (c). The ion-neutral collision frequency ν_{in} makes the drift-waves stable. In the saturated state, it is important to distinguish which kind of state, solitary drift wave or streamer, is formed, and co-existence of (2,1) and (3,1) modes or sole-existence of one dominant mode is related to the selection. The tendency in Fig. (b) and (c) shows some difference, and smaller B and larger ν_{in} is possible to give the condition for sole-existence of one dominant mode. In addition, it is necessary to consider the effect of the background distribution formation, which is self-consistently taken place by nonlinear transport processes. The ion-neutral collision frequency is also related to zonal flow damping, which gives a selection rule of turbulent structure formation [2]. By taking account both of the quasi-linear and nonlinear properties of the instabilities, the structural bifurcation observed in the experiment should be understood. In the solitary drift wave state, the steep gradient position is selected in accordance with the radial structure of the fundamental mode [5]. The mode structure is found to depend on the radial profile of the background density profile, so the selection will be investigated by nonlinear simulations with variation of the particle source profile.

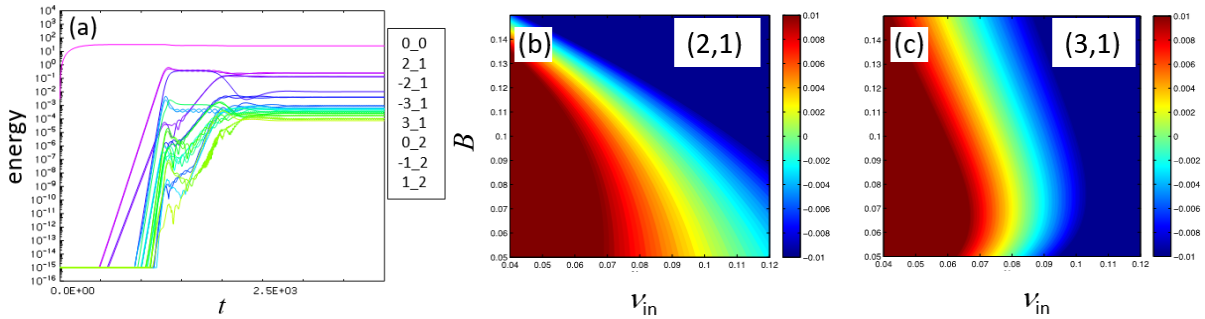

FIG. (a) Time evolutions of the energy of each Fourier component of the density fluctuation. Dependency of the growth rate on magnetic field strength B and ion-neutral collision frequency ν_{in} of (m, n) = (b) (2, 1) mode and (c) (3, 1) mode.

Acknowledgements

This work is supported by JSPS KAKENHI Grant Number JP24760703 and JP16K06938, by the collaboration program of NIFS (NIFS15KNST082, NIFS16KNXN323, NIFS13KOCT001) and of RIAM of Kyushu University.

References

[1] S. Oldenbürger, *et a*l. Plasma Phys. Control. Fusion **54**, 055002 (2012)
[2] N. Kasuya, *et al*. Phys. Plasma **15**, 052302 (2008)
[3] T. Yamada, *et al.*, Nature Phys. **4**, 721 (2008)
[4] H. Arakawa, *et al.*, Plasma Phys. Control. Fusion **51**, 085001 (2009)
[5] M. Sasaki, *et al*. Phys. Plasmas **22**, 032315 (2015)

Turbulence simulation of structural formation considering neutral particle profiles in linear devices

Satoshi Abe[1], Naohiro Kasuya [1,2], Makoto Sasaki [1,2], Yosuke Matsui [1], Shigeru Inagaki [1,2], Masatoshi Yagi [3]

1.Department of Advanced Energy Engineering Science, Interdisciplinary Graduate School of Engineering Sciences, Kyushu University

2. Research Institute for Applied Mechanics, Kyushu University

3.National Institute for Quantum and Radiological Science and Technology

6-1 Kasuga-koen, Kasuga, Fukuoka 816-8580, Japan

**E-mail: abe@riam.kyushu-u.ac.jp*

ABSTRACT

Fundamentals of turbulent transport have been studied using linear devices. Neutral particles play an important role in turbulent structural formation in the devices, so their effects are investigated by numerical simulations of linear device PANTA. Density profiles of neutral particles are calculated by a particle simulation using the Monte Carlo method. Then, the obtained profiles are introduced into a simulation code of resistive drift wave turbulence. Comparison of cases with the ion - neutral collision frequencies constant or not-constant in radius shows that non-uniformity of the neutral particle profiles can affect selection of fluctuation spectrum in the turbulent state in the linear devices.

KEY WORDS

turbulence, simulation, linear device, collisional plasma, neutral particle, drift-wave instability, structural formation.

1 INTRODUCTION

Turbulent transport is one of the keys for power generation by nuclear fusion, and basic experiments using linear devices are being conducted for the understanding [1]. It is known that control of neutral particles is important for the turbulent state in the linear devices, and structural bifurcation has been shown in the simulation of resistive drift wave turbulence with the neutral particle as the control parameter [2]. There are neutral particle distribution in the radial and axial direction, which must be taken into consideration. The purpose of this research is to evaluate effects of the neutral particle profile on the plasma turbulent structure. Numerical simulations of resistance drift wave turbulence are carried out with neutral particle profiles calculated by Monte Carlo method in a cylindrical plasma for that purpose.

2 SETUP FOR NUMERICAL SIMULATION

Basic researches on plasma turbulence have been carried out in linear device PANTA at Kyushu University [3]. Figure 1 shows the schematic of the device configuration. Argon plasmas are generated by helicon wave with device length ~ 4 [m] and plasma diameter ~ 10 [cm], plasma density at the center $n_0 \sim 1 \times 10^{19}$ [m^3] and the electron temperature $T_e \sim 3$ [eV]. Detailed analyses of plasma instability has been carried out. This plasma is the target for analysis in this research.

To calculate the neutral particle profile the particle code by the Monte Carlo method is used [4]. The Monte Carlo method is a numerical technique obtaining an approximate solution by iterative calculation using random numbers. The density and temperature profile of neutral particles are calculated, based on experimental parameters in PANTA. Particles are supplied from the production tube and exhausted by the pump. Reemission on the end plate and recombination in the plasma are considered. There are baffle plates installed in the linear device. Collisional processes between neutral particles, neutral particles - ions (elastic; exchange of momentum and charge), neutral particles - electrons (ionization) are taken into consideration. The weight of each neutral particle is calculated, associated with flight of the particle. The elastic collisions between neutral particles changes only their flight directions, and do not change energies and weights. The neutral - ion collisions affect the particle direction, but do not change the weights. The weights are changed only with ionization processes by collision with electrons. The test flight particles are traced until their weight become less than a defined threshold. If the pressure of the neutral particles in the device is sufficiently high and the effective ionization rate is low, the collisions between neutral particles plays an important role in determining the neutral particle distribution, so this process is calculated by iteration to obtain the nonlinear convergence.

To calculate the drift wave turbulence fluid code NLD is used [2]. The set of three-field simplified fluid equations including the effect of neutral particles is used to calculate the fluctuations of density N, electrostatic potential φ, and electron flow velocity in the magnetic field direction V. Spectral expansion with Fourier modes

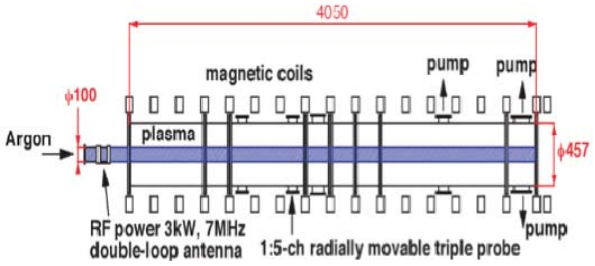

Fig.1 Schematic of linear device PANTA

are taken in the azimuthal and axial directions. By giving a particle source profile, nonlinear calculation is carried out to determine the self-consistent density distribution, and the relationship between excited modes and saturation states sustained by nonlinear couplings is studied.

3 RESULTS

3.1 Neutral Particle Profile

Firstly, two-dimensional neutral particle profiles are calculated using the Monte Carlo code. The profile with T_e = 3 [eV] and axial flow velocity normalized by the thermal velocity M = 0.3 is shown in Fig.2. The radial neutral particle profiles are obtained by averaging the two dimensional profile in the axial direction. The dependency on T_e and M is evaluated as in Fig.3. The neutral density in the radial direction is almost constant with the condition T_e = 3 [eV], but the higher electron temperature (T_e =5 [eV]) gives decrease of the density near the center and stronger density gradient, because of increase of the ionization rate. In addition, the larger axial flow gives decrease of the absolute value of the density. In this way, we obtained the difference of the neutral density profile depending on the plasma parameters.

3.2 Drift Wave Turbulence

We have calculated the neutral density profile, and is introduced in the calculation of drift wave instabilities. The profiles in the radial direction are almost constant in the case with T_e = 3 [eV], and small at the center, peaked near the plasma edge and almost constant outside the plasma with T_e = 5 [eV]. These profiles are fitted as the red lines A and B in Fig.3. The difference of the saturation states of drift wave turbulence using the ion - neutral collision frequency ν_{in} profiles considering the neutral profiles are calculated. Figure 4 shows the time evolutions of mode energies, where m and n are the azimuthal and axial mode numbers, respectively. In the case with constant ν_{in} = 0.06, the modes with (m, n) = (2,1) and (3,1) become dominant, and, (2,1) + (3,1) mode coupling forms a streamer [5] in the saturated state. With the profile B, the (2,1) mode is dominant, and the amplitude of the (3,1) mode becomes small, though this mode is linearly unstable. This selection is found to be related to the formation of the mean potential profile. In this way, it is found that non-uniformity of the neutral particle profiles can affect selection of dominant modes in the turbulent state in linear devices.

4 SUMMARY

The effects of neutral particle on structural formation of resistive drift wave turbulence in the linear device were investigated. The density profiles of neutral particles were calculated by a particle simulation, and the dependencies on the electron temperature and axial flow velocity were examined. As the electron temperature increases, the density profile becomes not flat in radius. As the result of introducing the neutral particle radial profile into the turbulence code, the formation of the mean potential acts to stabilize one of the modes, and gives selection of mode spectrum for saturation. In the future, quantitative analyses to find the selection rule on turbulent structure formation should be made.

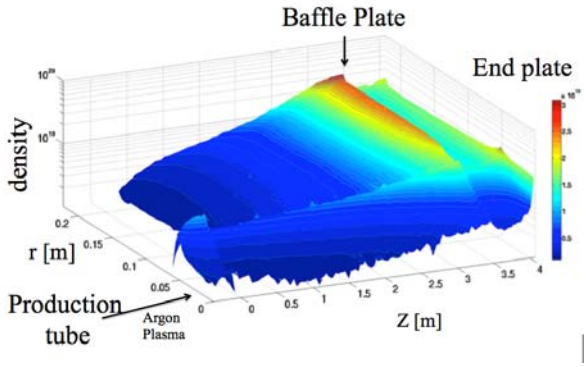

Fig.2 2-D neutral particle profile with T_e = 5 [eV] and M = 0.3.

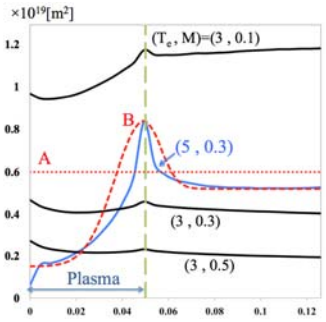

Fig3 Radial profiles of neutral particle density obtained by the Monte Carlo code. Fitted curves introduced into the turbulence code are also shown.

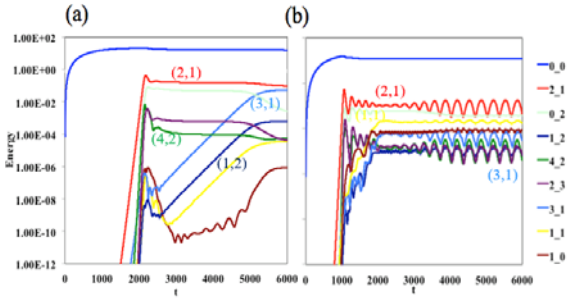

Fig.4 Time evolutions of fluctuation energies with (a) flat A and (b) non-flat B profiles in Fig. 3.

ACKNOWLEDGMENTS

This work is partly supported by JSPS KAKENHI Grant Numbers JP24760703 and JP16K06938, by the collaboration program of NIFS (NIFS15KNST082, NIFS16KNXN323, NIFS13KOCT001) and of RIAM of Kyushu University.

REFERENCES

1 G. R. Tynan, *et al.*, Plasma Phys. Control. Fusion **51** (2009) 113001.
2 N. Kasuya, *et al.*, Phys. Plasmas **15** (2008) 052302.
3 S. Inagaki, *et al.*, Sci. Reps. **6** (2016) 22189.
4 M. Ignatenko, *et al.*, Jpn. J. Appl. Phys. **46** (2007) 1080.
5 T. Yamada, *et al.*, Nature Phys. **4** (2008) 721.

Kinetic Simulation for Edge Plasma and Detached Divertor

T. Takizuka

Graduate School of Engineering, Osaka University

Kinetic effects play an important role in edge plasmas with steep gradient and including the open-field region. Complete kinetic behaviors can be simulated only by the kinetic modeling. One of the most powerful kinetic models is the particle simulation. The primary role of particle simulation is to clarify the fundamental physics and to establish a numerical model of the kinetic effect applicable to divertor codes with fluid modeling. Several results of PARASOL simulation for the kinetic effects in edge plasmas are presented.

1. Introduction

The detached divertor plasma is considered a solution for the heat control to reduce the divertor-plate erosion in fusion reactors with huge output power [1,2]. Synthetic reviews of the divertor plasma detachment will be published in a special issue of Plasma Physics and Controlled Fusion reviewing divertor plasma detachment in magnetic fusion devices [3].

There have been many experimental achievements on the detached divertor plasmas. To understand the physical mechanisms of the detachment observed in experiments, a lot of effort has been put into numerical studies using the comprehensive divertor simulation codes based on the plasma fluid modeling, SONIC, SOLPS, UEDGE, EDGE2D, EMC3-EIRENE etc. The agreement in the results between experiments and simulations has been rather fair but not satisfactory so far. Since these codes are widely applied in the predictive simulations for future fusion reactors, it is indispensable to improve the modeling in these codes.

Kinetic effect is one of key issues for improving the modeling for edge plasmas with steep gradient and including the open-field region. The mean free path is roughly given by l_{mfp0} [m] ~ $10^{16} \times T^2/n$ [eV^2/m^{-3}], which is comparable to the connection length of SOL plasma in a fusion reactor with possible parameters, L^{SOL} ~ 100 m, T ~ 300 eV, n ~ 4×10^{19} m^{-3} and l_{mfp0} ~ 20 m. Even in the detached divertor plasma, the kinetic effect by energetic particles still plays an important role. Assuming nT nearly constant along $\boldsymbol{B}$, l_{mfp} at an energy of E in the detached divertor region is estimated as l_{mfp} ~ $(T^{div}/T)\,(E/T)^2\,l_{mfp0}$. Considering a detached-divertor plasma with T^{div} ~ 2 eV near the divertor plate within the parallel connection length L^{detach} ~ 2 m, l_{mfp} becomes longer than L^{detach} for energetic particles with $E/T > 4$ ($E >$ 1.2 keV). These energetic particles directly arrive at the divertor plate. Plasma-wall interactions are influenced by the kinetic effects.

Several models of the kinetic effects are included into the plasma fluid equation, such as plasma-wall boundary conditions, heat transport coefficients parallel to $\boldsymbol{B}$ etc. Complete kinetic behaviors can be simulated only by the kinetic modeling. One of the most powerful kinetic models is the particle simulation [4-10]. The particle modeling for edge plasma simulations can easily treat the plasma-wall boundary conditions, and is very flexible in introducing A&M processes, compared with the continuum modeling of the Boltzmann equation. A review of the kinetic modeling for edge plasma and detached divertor will be found in the above special issue of PPCF [11]. In the present proceedings paper, several topics are picked up from this review article.

2. Particle simulation for whole SOL-divertor plasma

The particle model simulates the whole SOL and divertor plasmas including the sheath in front of the divertor plate. Although the system size L is much larger than the Debye length $\lambda_D = \sqrt{\varepsilon_0 T_e/e^2 n_e}$ in real plasmas, usual particle simulations, such as PARASOL [9-11], with the grid size of order of λ_D

are available to study such plasmas by setting artificially smaller values of $L/\lambda_D = 10^2 \sim 10^4$. This artificial setting is allowable because the characteristics of SOL/divertor plasmas under the quasi-neutral condition, except in the sheath region, are determined mainly by collisionality L/l_{mfp} and normalized ion Larmor radius ρ_{Li}/a but insensitive to the L/λ_D value as shown in Fig. 1. For divertor plasma simulations, the small L/λ_D value can be set by artificially elongating λ_D keeping the size L. The permittivity ε_0 in the Poisson equation, $-\nabla^2 \phi = e(\Sigma_i Z_i n_i - n_e)/\varepsilon_0$, is artificially enlarged for this sake. As an artificially elongated λ_D is used, we adopt, at the same time, a "collision cut-off technique" near the wall to keep the collisionless sheath condition valid.

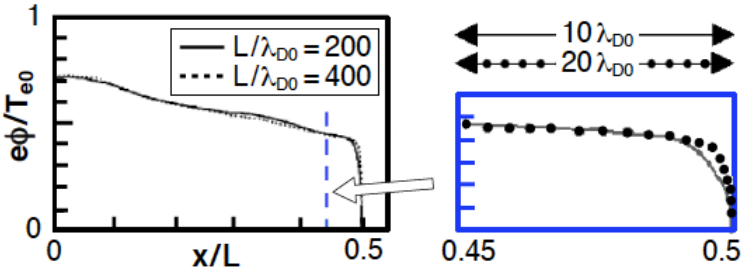

Fig. 1 Potential profiles for different L/λ_D values. The same profiles are established except for sheath region with the size of ~$3\lambda_D$.

We estimate the computation time t_{comp} necessary for a particle simulation. The total number of particles N_{tot} in a 1D system is L/Δ times of the mean number of particles in a cell N_{cell}, and it becomes $N_{tot} = (L/\Delta)^2 \times N_{cell}$ in a 2D system. The characteristic time τ for a SOL-divertor plasma equilibrium is L/C_s (C_s: sound speed), and the required time steps is $K_t \sim L/C_s\Delta t \sim \sqrt{m_i/m_e}(L/\Delta)$, because $v_{te}\Delta t \sim \Delta \sim \lambda_D$ in the particle simulation. Then t_{comp} is estimated as $t_{comp} = N_{tot} \times K_t \times \mathrm{FLO}_{\Delta t}$ / FLOPS ($\mathrm{FLO}_{\Delta t}$: number of floating-point operations for a single time-step advance of a particle, FLOPS: effective operating speed of a computer system). For example a small 1D case ($L/\Delta = 10^3$, $N_{cell} = 10^2$, $K_t = 10^5$, and $\mathrm{FLO}_{\Delta t} = 10^3$), it takes about 3 hours using a 1 GFLOPS computer. For a 2D case with parameters similar to the above, t_{comp} is still within several hours by the use of a 1 TFLOPS parallel computer. When we try a large and complex 2D system ($L/\Delta = 10^4$, $N_{cell} = 10^3$, $K_t = 10^7$, and $\mathrm{FLO}_{\Delta t} = 10^4$), t_{comp} becomes up to 100 days even if using a 1 PFLOPS massively parallel computer.

3. PARASOL simulation results of edge plasmas

3.1 Heat conduction parallel to the magnetic field

In the plasma fluid model, the heat conduction parallel to $\boldsymbol{B}$ is given by a collisional diffusive one, the Spitzer-Harm expression, $q_{//} = q_{SH} \equiv -\kappa_{//} \nabla_{//} T$. When $l_{mfp} > L_{//}$, $q_{//}$ is no more the diffusive transport but becomes the free-stream-like transport; $q_{//} = \alpha q_{FS} \equiv \alpha n T v_t$. To bridge the gap between short l_{mfp} case and long l_{mfp} case, a harmonic average has been applied; $1/q_{//} = 1/q_{SH} + 1/\alpha q_{FS}$. Here α is the flux-limiting coefficient, but this value is not conclusively obtained.

The α value is directly measured with the PARASOL simulation [12]. Hot plasma is supplied from the hot source region in the central SOL, and is lost to the divertor plates. Electron energy is cooled by radiation in the radiation cooling region near the plate (Fig. 2 (a)). For the various cases of collisionality $L_{//}/l_{mfp}$ ($10^{-3} \sim 10^3$) and radiation fraction f_{rad}, $q_{e//}$ for electron is measured in the intermediate region (Fig. 2 (b)). The PARASOL simulation results agreed with the classical theory, $q_{e//} = q_{SH}$, in the collisional regime, $L_{//}/l_{mfp} >> 1$. On the other hand in the collisionless regime, $L_{//}/l_{mfp} << 1$, $q_{e//}$ becomes much smaller than q_{SH}. When comparing $q_{e//}$ with q_{FS}, the ratio $q_{e//}/q_{FS}$ decreases in inverse proportion to $L_{//}/l_{mfp}$ in the collisional regime, while it saturates at a certain value in the collisionless regime. This saturated value was measured as α_e. It was found that the variety of α_e value is dependent on f_{rad}; $\alpha_e << 1$ for small f_{rad} ($T_e^{div} \sim T_e^{SOL}$) and $\alpha_e \sim 1$ for large f_{rad} ($T_e^{div} << T_e^{SOL}$) as shown in Fig. 2 (c).

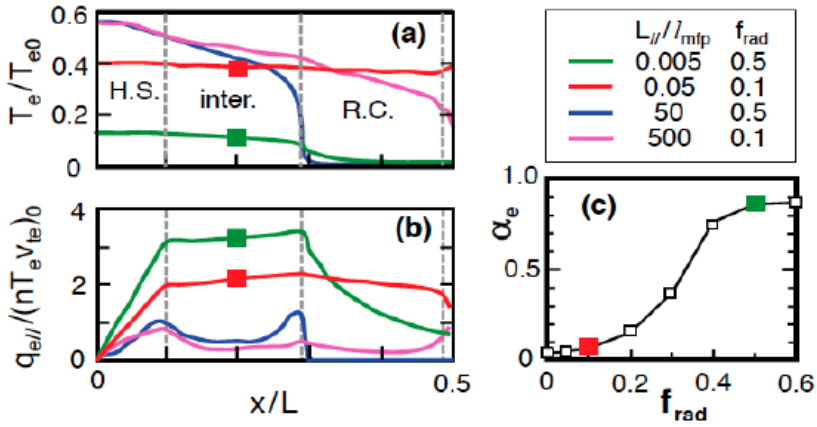

Fig. 2 Poloidal profiles of (a) T_e and (b) $q_{e//}$ for various cases of $L_{//}/l_{mfp}$ and f_{rad}. Hot electrons are supplied in the hot source (H.S.) region and cooled in the radiation cooling (R.C.) region. Flux limiting factor α_e measured in the intermediate region is shown in (c) as a function of f_{rad}.

3.2 SOL flow

The SOL flow pattern is varied by the null-point location in tokamak divertor plasmas. Many simulation studies on the SOL flow have been carried out using fluid codes, but the agreement with experiments were not satisfactory so far. PARASOL 2D simulation was carried out to clarify the physics of SOL flow pattern variation [13].

Figure 3 shows the 2D structures of $V_{//}$ in a tokamak with an aspect ratio A = 5.5 and the downward $V_{\nabla B}^{ion}$. The red region corresponds to the co-flow to the plasma current and the blue region corresponds to the counter-flow. The flow pattern is changed by the location of a null point (NP); the upper-null (UN) or the lower-null (LN) configurations. For the UN case with $V_{\nabla B}^{ion}$ away from NP (Fig. 3 (a)), $V_{//}$ is directed to the divertor plate both in the inner (high-field side, HFS) and outer (low-field side, LFS) SOL regions and the stagnation point ($V_{//}$ = 0) is located symmetrically at the bottom. On the other hand for the LN case (Fig. 3 (b)), $V_{//}$ in the outer SOL region has a backward flow pattern (red region). The stagnation point moves below the mid-plane of the outer SOL.

Based on these PARASOL simulation results, a new model for the edge plasma flow by introducing the "ion-orbit-induced flow" was presented [14]. Due to $V_{\nabla B}^{ion}$ in a tokamak, an ion with the co-$v_{//}$ is shifted outward (LFS), while an ion with the counter-$v_{//}$ is shifted inward (HFS). A banana orbit of a trapped ion drifted out from the core generates the co-flow (red region) in the outer SOL region. In a UN configuration, this "ion-orbit-induced flow" is additive to the original SOL flow towards the upper divertor plate in the outer SOL. On the contrary, in a LN configuration, the "ion-orbit-induced flow" is subtractive from the original SOL flow towards the lower divertor plate in the outer SOL. Transit ions as well play a role in the "ion-orbit-induced flow". This "ion-orbit-induced flow" causes the remarkable difference in flow patterns for the UN- and LN-divertor configurations.

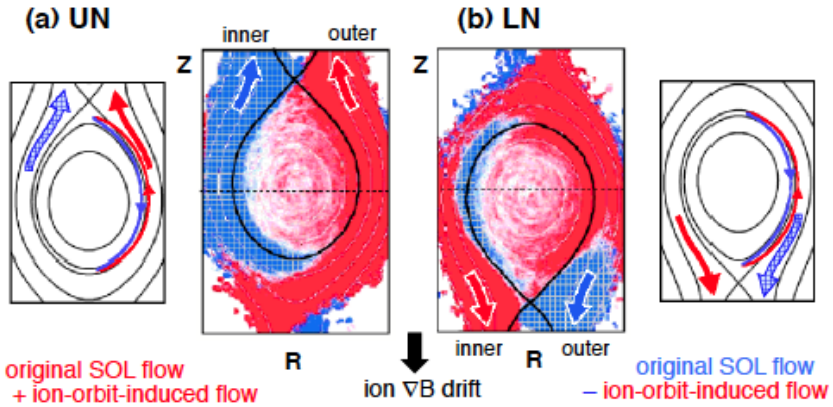

Fig. 3 Structures of $V_{//}$ in a tokamak with A = 5.5. For UN case (a), the "ion-orbit-induced flow" is additive to the original SOL flow towards the upper divertor plate in the outer SOL. For LN case (b), the "ion-orbit-induced flow" is subtractive from the original flow towards the lower plate in the outer SOL.

5. Summary and discussion

The particle simulation solving the full ion orbit is the closest to first principles, and has a high ability to understand the physics of edge plasmas and detached divertor. Although the kinetic effect becomes less important in the very collisional detached divertor region, the kinetic effect by energetic particles still plays an important role. In addition, the down-stream detached divertor plasma is influenced by the upstream SOL plasma, in which the kinetic effect is one of the essential factors.

Due to tremendous computational resources it seems too challenging for the particle simulation to work directly on the divertor design of future reactors. The primary role of the particle simulation is to clarify the fundamental physics and to establish a numerical model of the kinetic effect applicable to divertor codes with fluid modeling. Benchmark test between particle and fluid simulations before and after installing the kinetic-effect model is important. The second role is to study the whole tokamak of smaller size or in short time scale.

Time-separated integration of the codes can be a future project for the reliable design of tokamak-reactor divertor; 3D particle code for the turbulent diffusion in the shortest time scale (say ~1 ms), 2D particle code for the parallel transport in a shorter time scale (10~100 ms), 2D comprehensive divertor code to respond the sec order edge phenomena, and 1.5D transport code to follow fully the operation period.

Acknowledgements The author thanks many collaborators on the simulation and modeling for edge plasmas in fusion devices: Dr. K. Shimizu (QST), Dr. K. Hoshino (QST), Dr. N. Hayashi(QST), Dr. H. Kawashima (QST), Dr. M. Yagi (QST), Mr. M. Hosokawa (ITER), Dr. A. Loarte (ITER), Dr. A. Froese, Mr. S. Azuma, Dr. K. Ibano (Osaka U.), Dr. S. Togo (U. Tsukuba), Prof. A. Fukuyama (Kyorto U.), Prof. Y. Ueda (Osaka U.), and Prof. Y. Ogawa (U. Tokyo). Majority of simulation studies using PARASOL have been carried out at Japan Atomic Energy Agency, and some studies at Kyushu University, Kyoto University, and ITER organization.

References

[1] ITER Physics Basis, Chap. 4: Power and particle control, Nucl. Fusion **39** (1999) 2391.
[2] Progress in the ITER Physics Basis, Chap. 4: Power and particle control, Nucl. Fusion **47** (2007) S203.
[3] Reviewing divertor plasma detachment in magnetic fusion devices, edited by R. Maingi, T. Rognlien, to be published in Plasma Phys. Control. Fusion.
[4] R.W. Hockney, J.W. Eastwood, *Computer Simulation Using Particles* (New York, McGraw-Hill, 1981).
[5] C.K. Birdsall, IEEE Trans. Plasma Sci. **19** (1991) 65.
[6] R. Cohen, X.Q. Xu, Contrib. Plasma Phys. **48** (2008) 212.
[7] J.P. Verboncoeur, Plasma Phys. Control. Fusion **47** (2005) A231.
[8] D. Tskhakaya, K. Matyash, R. Schneider, F. Taccogna, Contrib. Plasma Phys. **47** (2007) 563.
[9] T. Takizuka, AIP Conf. Proc. **1237** (2010) 138.
[10] T. Takizuka, Plasma Sci. Technol. **13** (2011) 316.
[11] T. Takizuka, "Kinetic effects in edge plasma: kinetic modeling for edge plasma and detached divertor", to be published in Plasma Phys. Control. Fusion **59** (2017).
[12] A. Froese, T. Takizuka, M. Yagi, Plasma Fusion Res. **5** (2010) 026.
[13] T. Takizuka, K. Shimizu, N. Hayashi, M. Hosokawa, M. Yagi, Nucl. Fusion **49** (2009) 075038.
[14] T. Takizuka, K. Hoshino, K. Shimizu, M. Yagi, Contrib. Plasma Phys. **50** (2010) 267.

Research on behavior of divertor particle flux with a one-dimensional numerical model and an analytical one

Satoshi Togo, Tomonori Takizuka[a)], Makoto Nakamura[b)], Kazuo Hoshino[c)], Kenzo Ibano[a)], Yue Li[d)], Yuichi Ogawa[d)], Mizuki Sakamoto

Plasma Research Center, University of Tsukuba, 1-1-1 Tennodai, Tsukuba 305-8577, Japan
[a)]Graduate school of Engineering, Osaka University, 2-1 Yamadaoka, Suita 565-0871, Japan
[b)]National Institutes for Quantum and Radiological Science and Technology, 2-166 Omotedate, Obuchi-aza, O-aza, Rokkasho 039-3212, Japan
[c)]National Institutes for Quantum and Radiological Science and Technology, 801-1 Mukoyama, Naka 311-0193, Japan
[d)]Graduate School of Frontier Sciences, University of Tokyo, 5-1-5 Kashiwanoha, Kashiwa 277-8568, Japan

Behavior of particle flux at the divertor plate Γ_t as a function of that from the core plasma Γ_{sep} has been studied by using a one-dimensional fluid model and a reduced analytical one focusing on the effects of ion temperature anisotropy, radial width of the scrape-off-layer (SOL) and radial plasma diffusion. Bifurcation of Γ_t has been observed numerically and analytically. The effect of ion temperature anisotropy on Γ_t was small in the current calculation condition. In wider SOL case, the change of Γ_t became slower against Γ_{sep}. The region of multiple solutions became narrower in larger plasma radial diffusivity case.

1 Introduction

In order to design divertors which will escape serious damages due to the plasma particle flux, it is necessary to develop a numerical simulation code packages which can reproduce the detached divertor plasmas observed in experiments of existing torus devices. Numerical results on the behavior of the divertor particle flux from the conventional code packages, however, do not always agree with the experimental ones. Therefore, various effects, such as kinetic effects, supersonic flow, improved atomic and molecular processes and plasma wall interactions, have been studied in order to improve the numerical results of the conventional code packages [1–3]. Compared to these code packages, one-dimensional (1D) models are more convenient to gain physical insights because of its simplicity and short calculation time. In this paper, we studied the behavior of particle flux at the divertor plate Γ_t as a function of that from the core plasma Γ_{sep} by using a 1D fluid model [4–7] focusing on the effects of ion temperature anisotropy, radial width of the scrape-off-layer (SOL) and radial plasma diffusion in divertor (DIV) region. We also used a reduced analytical model in order to understand the structure of the numerical solutions.

2 Models

2.1 Numerical model

We have been developing a 1D fluid model of the SOL-DIV plasma and neutrals which distinguish between the parallel, $T_{i,\parallel}$, and perpendicular, $T_{i,\perp}$, components of ion temperature [4–7]. Because of the space limitation, we omit the explanations on the details of the fluid equations for the plasma and neutrals in this paper. The fluid equations and notations are the same as those used in Ref. [7]. In the isotropic T_i model, the following equations of parallel momentum transport and isotropic ion energy transport were solved in stead of the anisotropic ones;

$$\frac{\partial}{\partial t}(m_i n V) + \frac{\partial}{\partial s}\left(m_i n V^2 + n T_i + n T_e - \eta_i \frac{\partial V}{\partial s}\right) = M_m, \quad (1)$$

$$\frac{\partial}{\partial t}\left(\frac{1}{2} m_i n V^2 + \frac{3}{2} n T_i\right) + \frac{\partial}{\partial s}\left(\frac{1}{2} m_i n V^3 + \frac{5}{2} n T_i V - \kappa_i \frac{\partial T_i}{\partial s} - \eta_i \frac{\partial V}{\partial s} V\right) = Q_i + \frac{3 m_e}{m_i} \frac{n (T_e - T_i)}{\tau_e} - V \frac{\partial}{\partial s}(n T_e). \quad (2)$$

Here, η_i is the limited Braginskii ion parallel viscosity;

$$\eta_i = \frac{\eta_i^{Br}}{1 + \frac{\eta_i^{Br} \left|\frac{\partial V}{\partial s}\right|}{\beta n T_i}}, \ \eta_i^{Br} = 0.96 n T_i \tau_i, \quad (3)$$

where the limiting factor was set to be $\beta = 0.7$ according to Ref. [5]. The ion heat source term Q_i is given as follows;

$$Q_i = Q_i^{core} + \left(\epsilon_{FC} n_{n,recy} + \frac{3}{2} T_i n_{n,diff}\right)(\nu_{iz} + \nu_{cx}) - \left(\frac{1}{2} m_i V^2 + \frac{3}{2} T_i\right)(n_n \nu_{cx} + n \nu_{rc}) - \left(\frac{1}{2} m_i V^2 + g_i^{\perp} \frac{3}{2} T_i\right) \nu_{\perp}, \quad (4)$$

where the ion heat source from core plasma Q_i^{core} and radial diffusion frequency $\nu_{\perp} = D_{\perp}/d_{DIV}^2$ have non-zero

author's e-mail: togo@prc.tsukuba.ac.jp

values in SOL and DIV regions, respectively. The coefficient $g_i^{\perp}$, which represents the effect of radial heat diffusion, is set to be 3.

2.2 Reduced analytical model

In order to understand the structure of the numerical solutions and obtain steady state solutions including unstable ones, we have been developing an analytical model. This model is motivated by the fact that neutrals exist in a very thin region in front of the plate compared to the system length in the numerical results. In this model, reduced neutral equations are solved in homogeneous background plasma of density n, flow velocity V and single temperature T described by the sheath boundary conditions. For a given value of T and tentative total target heat flux P_t [W], total ion flux is given by $\Gamma_t = P_t/\gamma T$ [/s] where γ is the sheath heat transmission factor. Then, the flow velocity and density are estimated as $V = \sqrt{2T/m_i}$ and $n = \Gamma_t/2VA_{\parallel}$ where $A_{\parallel} = (d_{SOL}/L_{SOL})\, A_{sep} \sin\theta$ is the cross section of the flux tube normal to the magnetic field.

In the homogeneous plasma described above, the following reduced neutral equations are solved;

$$\frac{dn^{out}_{n,recy}}{dx} = -\frac{n^{out}_{n,recy}}{\lambda_r},\ \frac{dn^{inn}_{n,recy}}{dx} = \frac{n^{inn}_{n,recy}}{\lambda_r}, \tag{5}$$

$$-D_n \frac{d^2 n_{n,diff}}{dx^2} = -D_n \frac{n_{n,diff}}{\lambda_d^2} + n_{n,recy}\nu_{cx}. \tag{6}$$

Here, the volume recombination is neglected. The characteristic lengths, which are both constants for a given background plasma, are given as follows;

$$\lambda_r = \frac{V_{n,recy}}{\nu_{cx} + \nu_{iz} + \nu_{L,recy}},\ \lambda_d = \sqrt{\frac{D_n}{\nu_{iz} + \nu_{L,diff}}}. \tag{7}$$

The solutions to Eqs. (5) and (6) become

$$n_{n,recy} = n_{n,recy,t} \times \left[\exp\left(\frac{x-L}{\lambda_r}\right) + \exp\left(-\frac{x+L}{\lambda_r}\right)\right], \tag{8}$$

$$n_{n,diff} = f n_{n,recy} - f g n_{n,recy,t} \times \left[\exp\left(\frac{x-L}{\lambda_d}\right) + \exp\left(-\frac{x+L}{\lambda_d}\right)\right], \tag{9}$$

$$n_{n,recy,t} = \frac{V \sin\theta}{V_{n,recy} + (g-1)C_n f v_n} n, \tag{10}$$

$$f = \left(\frac{1}{\lambda_d^2} - \frac{1}{\lambda_r^2}\right)^{-1} \frac{\nu_{cx}}{D_n},\ g = \frac{D_n/\lambda_r + C_n v_n}{D_n/\lambda_d + C_n v_n}, \tag{11}$$

where L is the poloidal length from the stagnation point to the divertor plate. By integrating these neutral densities over x, the total number of the neutral particles are determined as follows;

$$N_{n,recy} = 2 n_{n,recy,t} \lambda_r A_{\parallel}/\sin\theta, \tag{12}$$

Table 1 Basic calculation conditions. The parentheses represent the compared ones.

Pitch angle θ	6°
Parallel system length $2L/\sin\theta$	44 m
Parallel SOL length $L_{SOL}/\sin\theta$	35.2 m
Parallel DIV length $L_{DIV}/\sin\theta$	4.4 m
SOL width d_{SOL}	1 (2) cm
DIV width d_{DIV}	5 cm
Separatrix surface area A_{sep}	40 m^2
Radial particle diffusivity $D_{\perp}$	0.5 (2) m^2/s
Carbon impurity fraction r_{imp}	0.01
Heat flux from core P_{sep}	4 MW
Ion flux from core Γ_{sep}	0.5-4.5×10^{22} /s
Ion temperature T_i	aniso. (iso.)

$$N_{n,diff} = 2 f n_{n,recy,t} (\lambda_r - g\lambda_d) A_{\parallel}/\sin\theta. \tag{13}$$

Particle fluxes from ionization, charge exchange, radial diffusion and core become as follows, respectively;

$$\Gamma_{iz,r} = N_{n,recy}\nu_{iz},\ \Gamma_{iz,d} = N_{n,diff}\nu_{iz}, \tag{14}$$

$$\Gamma_{cx,r} = N_{n,recy}\nu_{cx},\ \Gamma_{cx,d} = N_{n,diff}\nu_{cx}, \tag{15}$$

$$\Gamma_{\perp} = -2n\nu_{\perp} L_{DIV} A_{\parallel}/\sin\theta, \tag{16}$$

$$\Gamma_{sep} = \Gamma_t - \Gamma_{iz,r} - \Gamma_{iz,d} - \Gamma_{\perp}, \tag{17}$$

where L_{DIV} is poloidal length of DIV region. Heat fluxes from ionization, charge exchange, radial diffusion, impurity radiation and core become as follows;

$$P_{iz} = (\epsilon_{FC} - \epsilon_{iz})\Gamma_{iz,r} + \left(\frac{3}{2}T - \epsilon_{iz}\right)\Gamma_{iz,d}, \tag{18}$$

$$P_{cx} = \left[\epsilon_{FC} - \left(\frac{1}{2}m_i V^2 + \frac{3}{2}T\right)\right]\Gamma_{cx,r} - \frac{1}{2}m_i V^2 \Gamma_{iz,d}, \tag{19}$$

$$P_{\perp} = -\left(\frac{1}{2}m_i V^2 + 3g^{\perp}T\right)\Gamma_{\perp}, \tag{20}$$

$$P_{rad} = -2L_z(T)\, r_{imp} n^2 \lambda_d A_{\parallel}/\sin\theta, \tag{21}$$

$$P_{sep} = P_t - P_{iz} - P_{cx} - P_{\perp} - P_{rad}. \tag{22}$$

Then, the value of P_t is iteratively controlled such that obtained P_{sep} has the prescribed value.

3 Results

We investigated the effects of ion temperature anisotropy, SOL width d_{SOL} and radial particle diffusivity $D_{\perp}$ on the behavior of Γ_t as a function of Γ_{sep}. Table 1 shows the basic and compared calculation conditions we used. The results are shown in Fig. 1. For all calculation conditions, we obtained lower ($2 \times 10^{17} \sim 3 \times 10^{19}$ /m^3) and higher ($8 \times 10^{19} \sim 5 \times 10^{20}$ /m^3) density

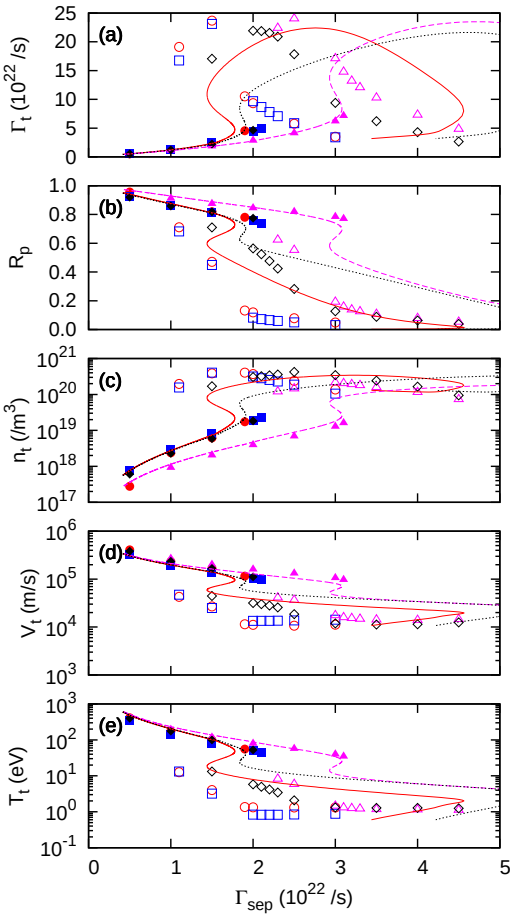

Fig. 1 (a) Particle flux Γ_t, (b) momentum flux amplification R_p, (c) density n_t, (d) flow velocity V_t and (e) (electron) temperature T_t at the sheath entrance as functions of particle flux from core plasma Γ_{sep}. Circular, square, triangular and rhombic symbols represent the numerical solutions with basic calculation condition, isotropic T_i, wider SOL width (d_{SOL} = 2 cm) and larger radial diffusivity $D_\perp$ = 2 m^2/s, respectively, where closed and open ones correspond to lower and upper stable solutions. Solid, broken and dotted lines stand for analytical solutions with basic calculation condition, wider SOL width and larger radial diffusivity, respectively.

branches of stable numerical solutions. Here, we call the former the lower solutions (closed symbols) and the latter the upper ones (open symbols) according to the way used in Ref. [8]. These branches share some range of Γ_{sep} (e.g. $1.1 \sim 1.9 \times 10^{22}$ /s for basic calculation conditions) and the actual branch of a solution depends on the branch the initial condition belongs to in this range. By using the reduced analytical model, we obtained S-shaped solutions. This kind of bifurcated behavior of the solutions agrees with those pointed out by earlier studies including the intermediate branch in the analytical solution which is not found by the numerical model because it is physically unstable [8,9]. Although the analytical solution well reproduced the numerical lower solutions, it did not reproduce the upper ones even qualitatively. This was because Eq. (21) remarkably underestimated the impurity radiation power. Improvement of the impurity radiation model in reduced analytical model is one of our future works. In the numerical upper solutions, we obtained the rollover of Γ_t which represents the onset of the detached plasma.

In the current calculation conditions, we did not observe a remarkable difference of the results from anisotropic and isotropic T_i models. This is due to the effects of ion parallel viscosity limitation for the lower solutions and the high collision frequency for the upper ones. With wider SOL width, the changes of Γ_t and other parameters became slower against Γ_{sep} because $A_\parallel$ became simultaneously large and required larger Γ_{sep} in order to make the same plasmas. In larger $D_\perp$ case, the solutions shifted like the wider SOL width case only for the upper ones because the radial diffusion was not large due to low density in the lower ones. Note that the region of multiple solutions became narrower in this case, which indicates much larger $D_\perp$ may extinguish that region.

4 Conclusion

We investigated the behavior of Γ_t as a function of Γ_{sep} by using a 1D fluid model and a reduced analytical one focusing on the effects of anisotropic T_i, radial width of the SOL and radial plasma diffusion. Bifurcation and rollover were observed in numerical solutions which were reproduced by the analytical model as for the lower ones. The effect of T_i anisotropy was small in the current calculation condition. In wider SOL case, the change of Γ_t became slower against Γ_{sep}. The region of multiple solutions became narrower in larger plasma radial diffusivity case.

Improvement of the impurity radiation model in reduced analytical model is one of our future works. In addition, we will study the effect of anisotropic T_i with more realistic conditions such as inhomogeneous magnetic field and finite plasma current.

References

[1] A.V. Chankin *et al.*, J. Nucl. Mater. **390-391** (2009) 319.
[2] K. Hoshino *et al.*, J. Nucl. Mater. **415** (2011) S549.
[3] M. Groth *et al.*, J. Nucl. Mater. **415** (2011) S530.
[4] S. Togo, *et al.*, J. Nucl. Mater. **463** (2015) 502.
[5] S. Togo, *et al.*, J. Comput. Phys. **310** (2016) 109.
[6] S. Togo, *et al.*, Contrib. Plasma Phys. **56** (2016) 729.
[7] S. Togo, *et al.*, Proc. 13th Burning Plasma Simulation Initiative (BPSI) Meeting (Kasuga, Japan 2015) 3-3.
[8] M. Sugihara, *et al.*, J. Nucl. Mater. **128-129** (1984) 114.
[9] H.X. Vu and A.K. Prinja, Phys. Fluids **5** (1993) 1809.

Vacancy cluster growth in tungsten induced by hydrogen

Kazuhito Ohsawa[1], Hideo Watanabe, Yuji Hatano[2], Masatake Yamaguchi[3]

[1]Research Institute for Applied Mechanics, Kyushu University
[2]Hydrogen Isotope Research Center, University of Toyama
[3]Center for Computational Science and e-system, Japan Atomic Energy Agency

1. Introduction

Divertor armor tiles installed in fusion reactors are exposed to the most intense plasma particle irradiation. So, it is planning that the divertor armor tiles are covered by tungsten (W) or its alloys because they have excellent properties as plasma facing materials (PFMs), e.g., low hydrogen (H) solubility and high melting point etc. However, a large amount of H isotope (D and T) retention has been reported in tungsten materials. In particular, tritium inventory is an important subject associated with safety of fusion reactors. H isotopes are not retained in W crystal lattice because of its low H solubility. However, H isotopes can be accommodated in vacancy and vacancy-type lattice defects. Stable configurations of multiple H atoms trapped in a W mono-vacancy have been reported in the previous works [1].

In the present paper, we pay attention to stable configurations of di-vacancy in W lattice and H atoms trapped in the di-vacancy. Beside, stability of the di-vacancy and vacancy-hydrogen (V-H) complex are investigated. Formation energy of di-vacancy is estimated to be negative. So, it is expected that di-vacancy nucleation does not take place [2]. On the other hand, V-H complexes combine because the binding energy is estimated to be positive. Therefore, the presence of H or H isotopes will enhance the growth of vacancy-type lattice defects.

2. Methodology

Nucleation of di-vacancy and binding of V-H complexes are investigated in terms of first-principle calculations on the basis of density functional theory. The calculations are performed by using Vienna ab initio simulation package (VASP) with PBE type potential. The cut-off energy of plane wave is 350eV. We used large simulation cell composed of 432 lattice points (6x6x6 BCC lattice) in the present calculations in order to reduce the effects of periodic boundary condition imposed on the simulation cell. Lattice relaxations are iterated until resultant force of each atom is lowered than 0.003 eV/Å. Binding energy is estimated, as follows.

$$E_B = 2\,\mathrm{E}[\mathrm{V}] - \mathrm{E}[\mathrm{V}_2] \tag{1}$$

$$E_B = \mathrm{E}[\mathrm{V}\mathrm{H}_m] + \mathrm{E}[\mathrm{V}\mathrm{H}_n] - \mathrm{E}[\mathrm{V}_2\mathrm{H}_{m+n}], \tag{2}$$

where V and H are represented vacancy and hydrogen, respectively. Integer *m* and *n* indicates the number of hydrogen atoms trapped in each vacancy and function E is the cohesive energy of the system including such lattice defects. Equations (1) and (2) indicate binding energies of two empty vacancies and V-H complexes, respectively. Positive binding energy indicates attractive interaction.

3. Results

We calculate binding energies between two vacancies at first and second nearest neighbors in a variety of BCC transition metals, that is, the two vacancies line up in the <111> or <100> direction. Fig. 1 shows the binding energies corresponding to stable di-vacancy structure. Di-vacancy of <111> arrangement is more stable for in Cr, Mo, and W, while di-vacancy of <100> arrangement is favorable in Fe. Fig. 1 also indicates binding energies of V-H complexes in the BCC metals. Stable configuration of di-vacancy hydrogen complex (V_2H_{12}) in Fe is <111> arrangement, that is, the di-vacancy structure changes as the number of H atoms increases in the di-vacancy.

Fig. 2 shows binding energies of V-H complexes in tungsten in detail. We investigate binding energies between V-H complex (V_1H_n) for *n*=1, 2, 3, and 6, where *n* is the number of H atoms trapped in a W vacancy. Di-vacancy hydrogen complex (V_2H_{2n}) is more stable than isolated V-H complex (V_1H_n). Only, the binding energy between two empty vacancies is estimated to be negative. Therefore, it is expected that the presence of H atoms enhances binding of isolated vacancies in W specimen.

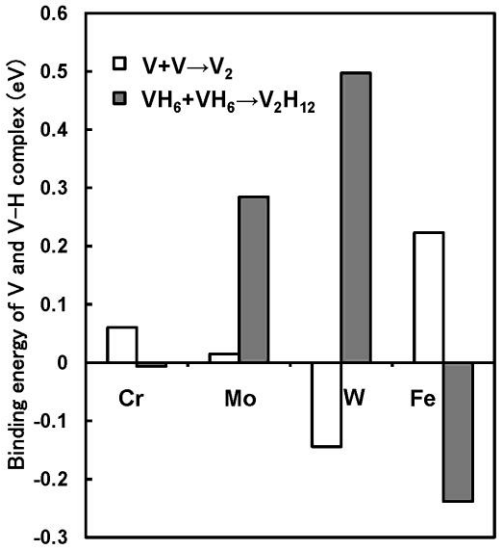

Fig. 1: Binding energies of vacancies and V-H complexes in BCC metals.

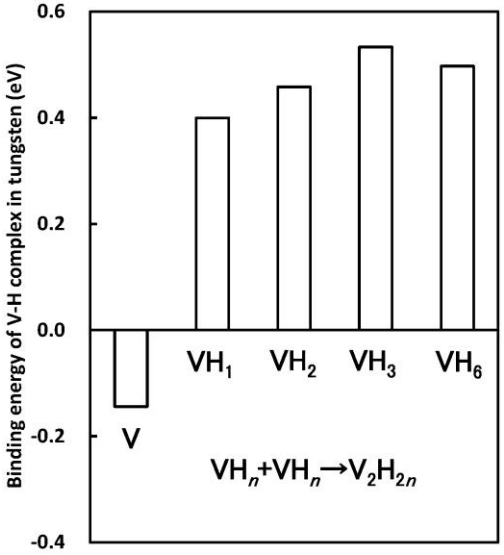

Fig. 2: Binding energies of a variety of V-H complexes in tungsten.

4. Discussion

In usual metals, vacancy cluster growth is observed by absorbing isolated vacancies in an appropriate high temperature. If formation energies of such vacancy-type lattice defects are assumed to be proportional to the surface area of the defects, these phenomena can be explained adequately. Vacancy clusters grow so as to reduce the formation energy. This assumption is supposed to be valid for many kinds of BCC transition metals, as shown in Fig. 1. However, di-vacancy formation in W will not take place exceptionally, according to the present works. On the other hand, V-H complexes in W can combine because the binding energies are positive. Fig. 3 is the schematic view of the effect of H on the vacancy binding in W lattice, that is, H atoms trapped in W vacancy enhances di-vacancy formation. Positron annihilation measurement is a sensitive experimental method to investigate vacancy-type lattice defects in metals. Usually, di-vacancy formation in metals is proved by drastic extension of the positron life-time at vacancy diffusion temperature. We hope that the behaviors of vacancies in W specimen will be revealed by such experiment.

In the previous paper, we pointed out an abnormal property associate with H atom structure in W vacancy. For example, symmetric octahedral structure is stable for six H atoms in usual BCC transition metals. However, an abnormal structure of H atoms was predicted in W vacancy, as shown in Fig. 4 [1]. Similarly, abnormal properties are expected associated with di-vacancy formation [2] and enhancement of vacancy cluster growth by H presence in W specimen. We do not conceive an appropriate reason why W materials have such abnormal properties but it will be an important subject of PFMs in the future.

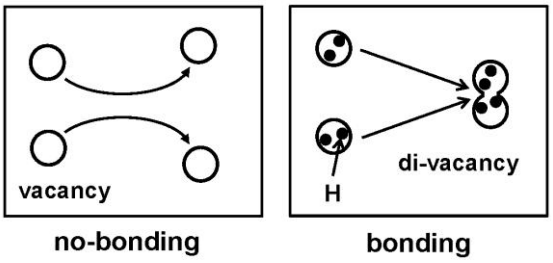

Fig. 3: Schematic view of binding of V and V-H complex in W specimen. It is predicted that Di-vacancy formation does not occur.

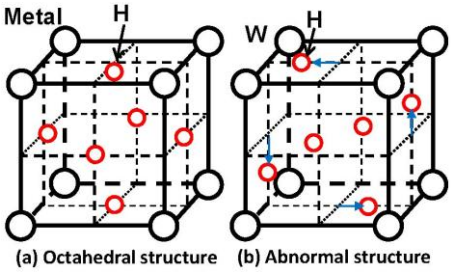

Fig. 4: (a) Octahedral structure of six hydrogen atoms in a vacancy. (b) Abnormal structure of H atoms.

References

[1] K. ohsawa *et al.*, Phys. Rev. B 85 (2010) 184117.

[2] L. Ventelon *et al.*, J. Nucl. Mat. 458 (2015) 187.

Simulation study on internal transport barrier formation using gyrofluid model

M. Yagi, Y. W. Cho[1], H. Seto and T. S. Hahm[1]

National Institutes for Quantum and Radiological Science and Technology,
Rokkasho Fusion Institute, Rokkasho, Aomori, Japan
[1]Seoul National University, Seoul 151-744, Republic of Korea

1. Introduction

To understand physical mechanism of transport barrier formation is a crucial issue for designing advanced operation scenario in JT-60SA and ITER. In QST, the project for multi-scale simulation with transport/MHD is going on. On MS_Turb Project (IFERC-CSC), the quasi-linear modification of neoclassical flows is taken into account for GF-ITG code and we revisit the internal transport barrier (ITB) formation investigated by Tokunaga et al[1]. We report the simulation results on ITB formation by the tuned heat source.

2. Model equations

GF-ITG code consists of three field equations (ion continuity equation, parallel momentum equation and ion temperature evolution equation)[1]

$$\frac{dW}{dt}+\kappa_n\frac{1}{r}\frac{\partial\Phi}{\partial\vartheta}+A\nabla_{//}V=\varepsilon_a\hat{\omega}_d F+\rho_*\frac{q}{\varepsilon}\mu_1\frac{1}{r}\frac{\partial}{\partial r}(rU_p)-\rho_*^2\mu\nabla_\perp^4 F \tag{1}$$

$$\frac{dV}{dt}=-A\nabla_{//}F+4\mu\nabla_\perp^2 V-\mu_1 U_p-A\sqrt{\frac{1}{\tau}}\frac{2}{5}\sqrt{\pi}\left|k_{//}\right|V+A\frac{2}{5}\frac{1}{\tau}\nabla_{//}T \tag{2}$$

$$\frac{3}{2}\left(\frac{dT}{dt}+\kappa_T\frac{1}{r}\frac{\partial\Phi}{\partial\vartheta}\right)-\left(\frac{dn}{dt}+\kappa_n\frac{1}{r}\frac{\partial\Phi}{\partial\vartheta}\right)=\frac{5}{2\tau}\varepsilon_a\hat{\omega}_d T-\frac{9}{5\sqrt{\pi}}A\left|\nabla_{//}\right|T+\frac{2}{5}A\nabla_{//}V+\chi_\perp\nabla_\perp^2 T+S_T\delta_{0,0} \tag{3}$$

where $W=n-\nabla_\perp^2 F$, $n=\Phi-\langle\Phi\rangle$, $F=\Phi+p/\tau$, $p=n+T$. The magnetic curvature operator is given by

$$\hat{\omega}_d=2\cos\vartheta\frac{1}{r}\frac{\partial}{\partial\vartheta}+2\sin\vartheta\frac{\partial}{\partial r} \tag{4}$$

The poloidal flow is given by

$$U_p=V+\rho_*\frac{q}{\varepsilon}\frac{\partial}{\partial r}\left(F-\kappa_{nc}T\right) \tag{5}$$

The neoclassical viscosities are given by[2,3]

$$\mu_1=\frac{0.66\varepsilon^{1/2}\nu_i}{(1+1.03\nu_{*i}^{1/2}+0.31\nu_{*i})(1+0.66\varepsilon^{3/2}\nu_{*i})} \tag{6}$$

$$\kappa_{nc} = \frac{1}{1+\nu_{*i}^2\varepsilon^3}\left(\frac{1.17-0.35\nu_{*i}^{1/2}}{1+0.7\nu_{*i}^{1/2}} - 2.1\nu_{*i}^2\varepsilon^3\right) \quad (7)$$

For the normalization, Bohm time $t_B = a^2/\chi_B, \chi_B = cT_e/eB$ and the minor radius a are used [1].

3. Quasi-linear effect on transport

In the previous study [4], we have neglected the quasi-linear (QL) term in the convective nonlinearity of density assuming the effect is small, namely $[\Phi, n] = 0$, where $n = \Phi - \langle\Phi\rangle$. However, for $m \neq 0$ and $n \neq 0$, the term $[\Phi, n]_{m,n} = \frac{d\Phi_{0,0}}{dr} ik_\theta \Phi_{m,n}$ appears in Eqs.(1) and (3). Figure 1 shows the time evolution of ion temperature profile. The dependence of quasi-linear effect on transport at $t = 5$ is shown. In the simulation, the Gaussian type of the heat source $S = Pexp(-(r - S_r)^2/\Delta^2)$ with $P = 2.0, S_r = 0.4, \Delta = 0.05$ is applied at $t = 2$ (shown by the dashed curve) then, the time evolution of ion temperature profile is examined. Note that the neoclassical ballooning mode (NBM) is turned off for this case. It is found that the QL effect is small contribution around ITB region for the case without NBM.

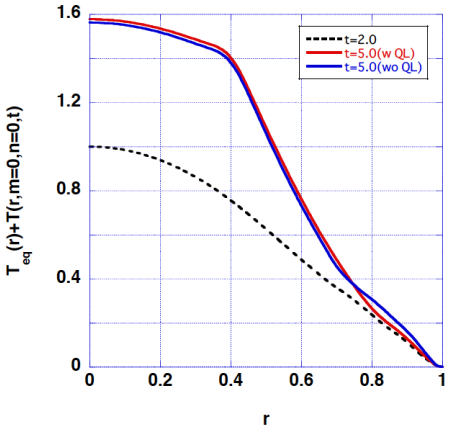

Fig.1 Time evolution of ion temperature profile.

4. Dependence of heat source location on ITB formation

Next, we examine the dependence of heat source location on ITB formation. In this simulation, the QL effect of the convective nonlinearity of density is NOT taken into account. The source location is controlled by the parameter S_r. Figure 2 shows the heat source profile. 5 cases with $S_r = 0,03,0.4,0.5,0.6$ are investigated. Figure 3 shows the ion temperature profile at $t = 12$ for each case. In this case, the heat source is applied at $t = 5$ (shown by the dashed curve). It is found that the weak ITB forms for $S_r = 0.4$. Note that the q minimum position is located

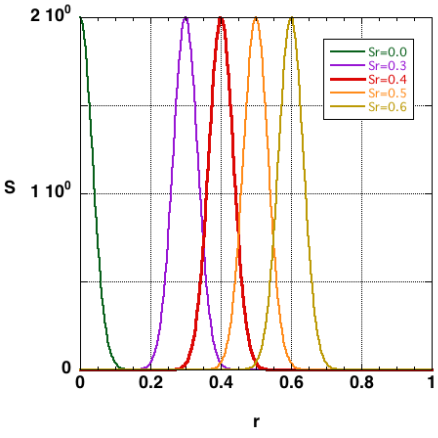

Fig.2 Heat source profile.

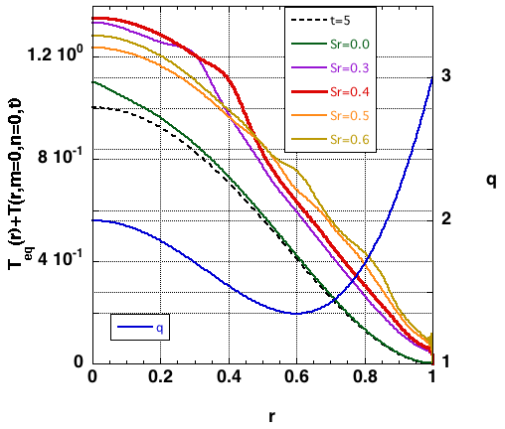

Fig.3 Time evolution of ion temperature profile for each location of heat source.

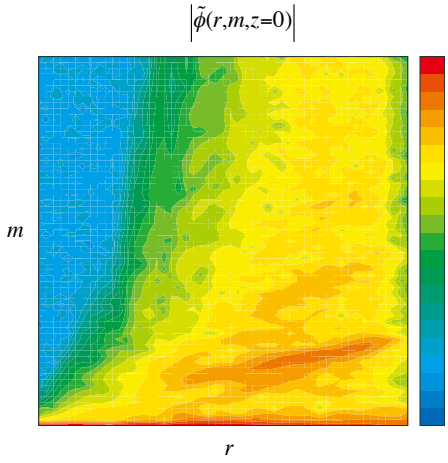

Fig.4 Turbulence intensity on (r,m) space.

at $r = 0.6$ (shown by the blue curve). Figure 4 shows the turbulence intensity (in the logarithmic scale) at $t = 20$ on (r,m) space. It is seen that inside of ITB, the turbulence is suppressed, on the other hand, the low m modes develop outside of ITB which produce the large convection.

5. Discussion

We perform the flux driven simulation taking account of the QL modification of neoclassical flows and investigate the time evolution of ion temperature profile. At first, the effect of QL term in the convective nonlinearity of the density is examined. It is shown that this effect is negligible around ITB region if NBM is not taken into account. Then, we investigate the dependence of heat source location on ITB formation. A new finding is that the weak ITB is formed when the Gaussian type heat source is applied at $r = 0.4$.

Acknowledgments

The author would like to thank Drs. N. Miyato, A. Matsuyama and T. Takizuka for useful comments. The computation was carried out using the HELIOS supercomputer system at IFERC-CSC.

References

[1] S. Tokunaga et al., Nucl. Fusion 49 075023(2009).

[2] J. D. Callen et al., Plasma Physics and Controlled Nuclear Fusion Research (International Atomic Energy Agency, Vienna, 1987), Vol. I, p. 157; μ_1 is given here.

[3] F. L. Hinton and R. D. Hazeltine, Rev. Mod. Phys. 48 239(1976); κ_{nc} is given by eq.(6.136).

[4] M. Yagi, H. Seto, Y. W. Cho and T. S. Hahm, the procs of 13th Burning Plasma Simulation Initiative (BPSI) Meeting, Dec. 10-11, 2015, Kyushu Univ., Kasuga, Japan. http://www.riam.kyushu-u.ac.jp/sosei/bpsi/bpsi13.html

Linear analysis of non-ideal ballooning mode instability with real electron inertia

H. Seto and M. Yagi

National Institutes for Quantum and Radiological Science and Technology, 2-166 Obuchi-Omotedate, Rokkasho-mura, Aomori, 039-3212, Japan

Shaping effects on non-ideal ballooning mode instabilities are numerically investigated by the use of two different geometries, a shifted circular and a D-shape equilibrium, with the same pressure shear and magnetic shear profile based on a linearized Grad-Shafranov equilibrium. The result is consistent with a local analysis indicating that the ellipticity $\kappa > 1$ stabilizes ballooning-type instabilities (BIs) by weakening the poloidal magnetic curvature and the positive triangularity $\delta > 0$ may also stabilize BIs by deepening the magnetic well on the bad curvature plane.

1 Introduction

The H-mode discharge operation [1] is indispensable for a DEMO reactor from the view point of the confinement efficiency but the intermittent large heat flux driven by edge localized modes should be avoided for the engineering constraint of the heat load on plasma facing components [2]. It is therefore one of the important issues to understand shaping effects on the edge plasma stability, since the ellipticity $\kappa > 1$ and the positive triangularity $\delta > 0$ improve the plasma confinement property. According to a local analysis of shaping effects on the current diffusive ballooning mode instability [3], the ellipticity stabilizes the ballooning-type instabilities (BIs) explicitly by weakening the poloidal magnetic curvature and the positive triangularity may also stabilize BIs implicitly by deepening the magnetic well on the bad curvature plane.

In this paper, impacts of shaping effects on the non-ideal ballooning modes (NIBMs) are numerically investigated by BOUT++ code [4] with two different geometries that have the same pressure shear and the magnetic shear profile. One has a shifted circular geometry and the other has a D-shaped geometry and the both are based on a linearized Grad-Shafranov equilibrium (LGSE) [5]. For describing NIBMs, we employ a 3-field reduced MHD model consisting the resistive ballooning mode (RBM) [6,7] and the collisionless ballooning mode (CBM) [8,9], where the other non-ideal effects are neglected [10].

The rest of this paper is organized as follows. In section 2, brief descriptions of the LGSE and the 3-field RBM/CBM model are given. Section 3 gives simulation results and a summary.

2 Analytic equilibrium model and 3-field RBM/CBM model

The Grad-Shafranov equation Eq.(2.1) is a nonlinear partial differential equation (PDE) for the poloidal flux function ψ requiring two flux functions such as the pressure gradient $dp/d\psi$, the flux function $IdI/d\psi$,

$$R^2\nabla\cdot\left(\frac{1}{R^2}\nabla\psi\right) = \mu_0 R^2\frac{\mathrm{d}p}{\mathrm{d}\psi} - I\frac{\mathrm{d}I}{\mathrm{d}\psi}, \tag{2.1}$$

where R is the major radius and μ_0 is the permeability in vacuum. For comparison with the analytic analysis, an analytic solution of Eq.(2.1) with the fixed $p(r)$ and $q(r)$ profile is desirable, where r is the minor radius. To linearize Eq.(2.1), we define Fourier series for all quantities and expand them with respect to the inverse aspect ratio $\varepsilon = r/R$. With these approximations, the horizontal position R and the vertical position Z can be expressed with respect to non-orthogonal torus (NOT) coordinates (r, ϑ, ζ),

$$R(r,\vartheta) = R_{\mathrm{ax}}\left(\varepsilon^0 1 - \varepsilon^1\frac{r}{R_{\mathrm{ax}}}\cos\vartheta - \varepsilon^2\frac{\Delta(r)}{R_{\mathrm{ax}}} - \varepsilon^2\sum_{k=2}^{\infty}\frac{S_k(r)}{R_{\mathrm{ax}}}\cos\left[(k-1)\vartheta\right] + \mathcal{O}(\varepsilon^3)\right), \tag{2.2}$$

$$Z(r,\vartheta) = R_{\mathrm{ax}}\left(\varepsilon^1\frac{r}{R_{\mathrm{ax}}}\sin\vartheta - \varepsilon^2\sum_{k=2}^{\infty}\frac{S_k(r)}{R_{\mathrm{ax}}}\sin\left[(k-1)\vartheta\right] + \mathcal{O}(\varepsilon^3)\right), \tag{2.3}$$

where the subscript "ax" stands a value at the magnetic axis, $\Delta(r)$ is the Shafranov shift defined to be $\Delta(0) = 0$, $S_k(r)$ is the shaping coefficients, ϑ is the poloidal angle and ζ is the geometrical toroidal angle. The red colored tags ε^n show that labeled terms are assumed to be n-th order with respect to ε.

By the use of these orderings, the nonlinear PDE (2.1) can be finally expanded into the following Fourier series of linearized ordinary differential equations (ODEs) [5],

$$\cos(0\vartheta): \quad I_2'(r) + \frac{r(2-s)}{q^2 R_{\rm ax}^2} + \frac{\beta'}{2} = 0, \quad \beta(r) = \frac{p(r)}{B_{\rm ax}^2/2\mu_0}, \quad \boldsymbol{B}(r,\vartheta) = \nabla\zeta \times \nabla\psi + I\nabla\zeta \tag{2.4}$$

$$\cos(1\vartheta): \quad \frac{\mathrm{d}}{\mathrm{d}r}\left(\frac{r^3}{q^2}\Delta'\right) + \frac{r}{R_{\rm ax}}\left(R_{\rm ax}^2 r\beta' - \frac{r^2}{q^2}\right) = 0, \tag{2.5}$$

$$\cos(k\vartheta): \quad S_k''(r) + \frac{3-2s}{r}S_k'(r) + \frac{1-k^2}{r^2}S_k(r) = 0 \quad \text{for } k \geq 2, \tag{2.6}$$

where $'$ stands derivatives with respect to r and $I_2(r)$ is the 2nd-order correction for the flux function I, $\boldsymbol{B}$ is the magnetic field. Eq.(2.4) and Eq.(2.5) are 1st-order ODEs, where the former describes the radial force balance and the latter yields the Shafranov shift profile $\Delta(r)$. Eq.(2.6) is the 2nd-order ODE determining the shaping coefficient profile $S_k(r)$. If the safety factor is defined by $q(r) = q_0 + q_1(r/r_1)^l$, Eq.(2.6) has analytic solutions satisfying a boundary condition $S_k(a)$ at $r = a$ and a non-singular condition at $r = 0$,

$$S_k(r) = S_k(a)\frac{r^{k-1}{}_2F_1(\alpha_{kl}, \beta_{kl}; \gamma_{kl}; -(q_1/q_0)(r/r_1)^l)}{a^{k-1}{}_2F_1(\alpha_{kl}, \beta_{kl}; \gamma_{kl}; -(q_1/q_0)(a/r_1)^l)}, \tag{2.7}$$

$$\alpha_{kl} = -1 + \frac{k}{l} - \sqrt{\frac{k^2}{l^2} - \frac{2}{l} + 1}, \quad \beta_{kl} = -1 + \frac{k}{l} + \sqrt{\frac{k^2}{l^2} - \frac{2}{l} + 1}, \quad \gamma_{kl} = 1 + 2\frac{k}{l}, \tag{2.8}$$

where a is the radial position of the last closed flux surface and ${}_2F_1(a, b; c; z)$ is the hypergeometric function. It is notable that relations between $S_k(a)$ and well-known shaping factors are roughly written by

$$S_2(a) \simeq a\frac{1-\kappa}{1+\kappa}, \quad S_3(a) \simeq -\frac{a\delta}{4}, \tag{2.9}$$

where the squareness $S_4(r)$ and the other higher mode coefficients have been neglected.

BOUT++ code uses field-aligned coordinates (x, y, z) [11] based on the local orthogonal flux (LOF) coordinates (ψ, θ, ζ) rather than the NOT coordinates [4], where θ is the poloidal angle in the LOF coordinates. A coordinate transform from the LOF to the NOT coordinates is, therefore, required to generate shaped equilibriums with the LOF coordinates by the use of Eqs.(2.2)-(2.9). For the radial coordinates label, the relation between $\psi(r)$ and $r(\psi)$ is obtained by solving Eq.(2.10) in the NOT coordinates,

$$\frac{\mathrm{d}\psi}{\mathrm{d}r} = \frac{I}{2\pi q}\oint d\vartheta \frac{1}{R}\left(\frac{\partial Z}{\partial r}\frac{\partial R}{\partial \vartheta} - \frac{\partial R}{\partial r}\frac{\partial Z}{\partial \vartheta}\right). \tag{2.10}$$

The NOT poloidal angle with respect to the LOF coordinates $\vartheta(\psi, \theta)$ is then evaluated from

$$\vartheta(\psi,\theta) = \theta - \int_r^{r_{\rm outer}} \frac{\partial\vartheta}{\partial r}dr, \quad \frac{\partial\vartheta}{\partial r}(\psi,\theta) = \frac{\nabla r\cdot\nabla\vartheta}{\nabla r\cdot\nabla r}, \quad r_{\rm outer} = r(\psi_{\rm outer}), \tag{2.11}$$

where the boundary condition $\vartheta(\psi_{\rm outer}, \theta) = \theta$ has been applied implicitly.

To evaluate the impact of shaping effects on NIBMs, we employ the linearized RBM/CBM model [10]

$$\frac{\partial}{\partial t}\frac{\nabla_\perp^2\phi_1}{B_0^2} = -B_0^2\nabla_\parallel\frac{\nabla_\perp^2 A_{\parallel 1}}{B_0} + \boldsymbol{b}_0\times\boldsymbol{\kappa}_0\cdot\nabla p_1, \tag{2.12}$$

$$\frac{\partial p_1}{\partial t} = -\frac{\boldsymbol{b}_0\times\nabla_\perp\phi_1\cdot\nabla_\perp p_0}{B_0}, \tag{2.13}$$

$$\frac{\partial}{\partial t}\left(A_{\parallel 1} - d_e^2\nabla_\perp^2 A_{\parallel 1}\right) = -\nabla_\parallel\phi_1 + \eta\nabla_\perp^2 A_{\parallel 1}, \tag{2.14}$$

where t is the time, ϕ is the electrostatic potential, $A_\parallel$ is the parallel vector potential, $\boldsymbol{\kappa}$ is the magnetic curvature, d_e is the electron skin depth, η is the resistivity. In Eqs.(2.12)-(2.14), the subscript '0' stands the equilibrium part, the subscripts '1' stands the perturbed part of physical quantities normalized with poloidal Alfvén unit respectively. As described before, the other non-ideal effects are neglected for simplicity.

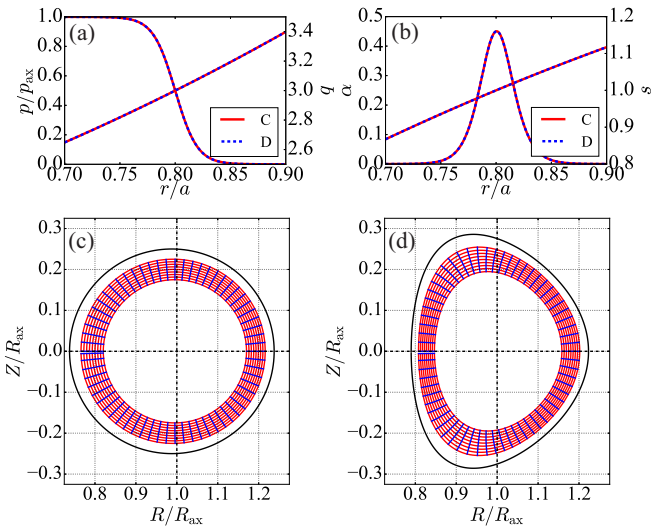

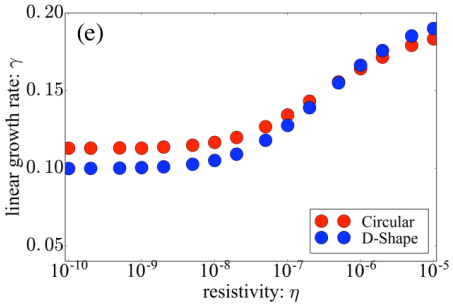

Fig.(a): pressure and safety factor profiles
Fig.(b): pressure and magnetic shear profiles
Fig.(c): shifted circular equilibrium
Fig.(d): D-shaped equilibrium ($\kappa \sim 1.3, \delta \sim 0.3$)
Fig.(e): resistivity dependence of growth rate of n=80 CBM/RBM for two geometries

3 Simulation results and summary

Figs.(a)-(d) show the shifted circular and the D-shaped equilibrium with the same pressure and safety factor profile based on the LGSE, where we have used following parameters for the both equilibriums, $R_{\rm ax} = 2.0$ [m], $a = 0.5$ [m], $B_{\rm ax} = 2.0$[T], $0.7 \le r/a \le 0.9$, $\beta_{\rm ax} = 5.0\times10^{-4}$, $p(r)/p_{\rm ax} = 0.5(1-\tanh[50(r/a-0.8)])$, $q(r) = 1.5 + 1.5(r/0.8a)^2$. The peak of the pressure shear factor is $\alpha = -q^2 R_0 \beta' \sim 0.45$ at $r/a = 0.8$ and the corresponding magnetic shear factor $s = (r/q)q' \sim 1$, which is ideally stable since the ideal stability boundary is $\alpha_{\rm crit} \sim 0.6s \sim 0.6$. We employ equally spaced grids for 1/80 sector of torus, where the grid widths in directions perpendicular to the magnetic field line are about 10 times finer than characteristic lengths relevant to the electron skin depth.

The shaping effects on the $n = 80$ CBM/RBM growth rate are summarized in Fig.(e). Since the resistivity regime relevant to the edge plasma lies roughly from $\eta \sim 10^{-9}$ for $T_e \sim 10^3$ [eV] to $\eta \sim 10^{-7}$ for $T_e \sim 10^2$ [eV], the ellipticity and the triangularity can stabilize NIBMs and their stabilizing effects become stronger in the collisionless regime where CBM is dominant and its growth rate is almost independent of the resistivity.

Acknowledgement

This work is partly supported by MEXT KAKENHI Grant No. 16K18342. Computations were carried out on the Helios supercomputer at the Computational Simulation Centre of the International Fusion Energy Research Centre (IFERC-CSC).

Reference

[1] F. Wagner *et al.*, Phys. Rev. Lett. **49**, 1408 (1982), [2] N. Asakura *et al.*, Nucl. Fusion **53**, 123013 (2013), [3] M. Yagi *et al.*, J. Phys. Soc. Jpn. **66**, 379 (1997), [4] B.D. Dudson *et al.*, J. Plasma Phys. **81**, 365810104 (2015), [5] J.P. Graves, Plasma Phys. Control Fusion **55**, 074009 (2013), [6] B.A. Carreras *et al.*, Phys. Rev. Lett. **50**, 503 (1983), [7] L. Garcia *et al.*, Phys. Plasmas **6**, 107 (1999), [8] F. Porcelli, Phys. Rev. Lett. **66**, 25 (1991), [9] J.W. Conner, Plasma Phys. Control. Fusion **35**, 757 (1993), [10] H. Seto *et al.*, Plasma Fusion Res. **11**, 1203122 (2016), [11] M.A. Beer et al., Phys. Plasmas **2**, 2687 (1995).

Particle simulation of plasma heating and production by electron cyclotron waves in tokamak plasmas

Tomohide Ikeda, Atsushi Fukuyama
Graduate School of Engineering, Kyoto University

1 Purpose

Plasma production by electron cyclotron waves has been conducted in tokamak, though the physics mechanism has not been understood well. Various phenomena are coupled with each other - electron accelation at the elecron cyclotron resonance, ionization by collisions with neutral particles, current drive by toroidal electric field and electron cyclotron waves, suppresion of particle losses by vertical magnetic field, and production of closed magnetic configuration. In order to analyze these pheomena self-consistently, we are developing particle simulation model.

2 Simulation model

Based on the two-dimentional electrostatic particle code pic2des_p[1], we have extended the velocity space to three dimention and make it possible to describe electromagnetic waves by Maxwell's equation. The procedure of simulation is as follows: set position and velocity of particles, calculate the current density on grid, solve normalized Maxwell's equation to obtain the electric field $\boldsymbol{E}$ and the magnetic field $\boldsymbol{B}$ at the particle position, and solve relativitic equation of motion. Furthremore, to avoid the reflection of electromagnetic waves at boundary, no-reflection boundary condition and vacuum region near the boundary are assumed. In the following simulation, time and space is normalized by typical plasma frequency and Debye length respectively, and the ratio of the light speed and the electron thermal speed is assumed to be 10.

3 Simulation result

First, we show the propagation of electromagnetic waves excited by waveguide in vacuum. The two dimentional structure of electric field E_y is shown in Fig 1. Horizontal axis and vertical axis are in the x and y direction respectively. No reflection of waves at boundary was confirmed.

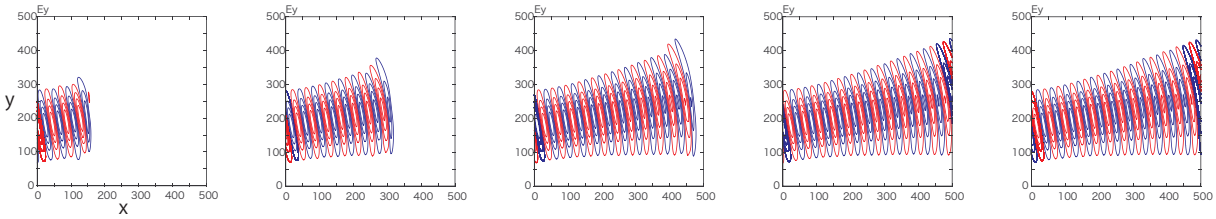

$\bar{t} = 16$ $\bar{t} = 32$ $\bar{t} = 48$ $\bar{t} = 60$ $\bar{t} = 72$

Fig 1: The propagation of electromagnetic waves in vaccum without reflection at the boundary

Next, linear plasma density is assumed and the reflection at the cutoff where the plasma frequency equal to the wave frequency. In a plasma the average number of electrons and ions per cell are 32, and it is assumed that the density increase linearly in the x direction, with $\bar{n}(x = 0) = 0.5$ and $\bar{n}(x = 500) = 1.5$, and the wave frequency $\bar{\omega}$ is 1.0. Reflection of the EM wave at the cutoff $\bar{n} = 1$ is shown in Fig 2.

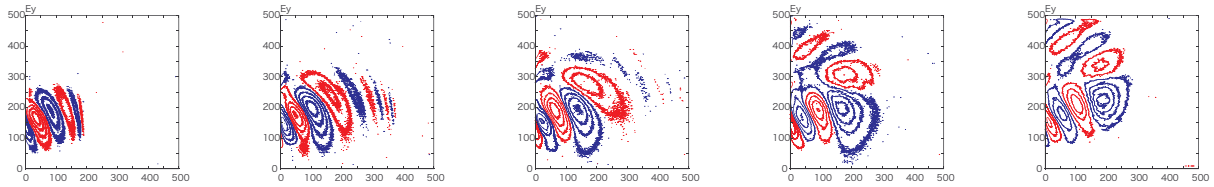

Fig 2: Reflection of electromagnetic waves at the plasma cutoff

Finally, static magnetic field which incleases linearly in the x direction is introduced, and X mode waves are excited from the weak magnetic field side. The magnitude of the static magnetic field $\bar{B}_y(0) = 4.0$, $\bar{B}_y(500) = 8.0$ and the wave frequency $\bar{\omega} = 6.0$. Cylotron resonance is located at $x \sim 250$. Time evolution of the spatial profile of wave's electromagnetic field is shown in Fig 3, and the electron temperature is shown in Fig 4.

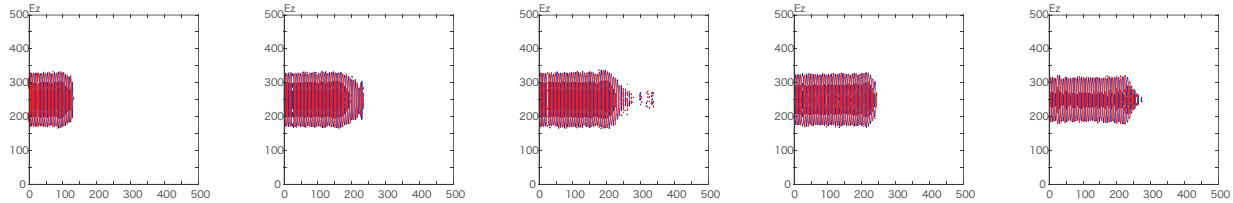

Fig 3: Time evolution of spatial structure of wave electromagnetic field : absorption by cyclotron resonance is observed

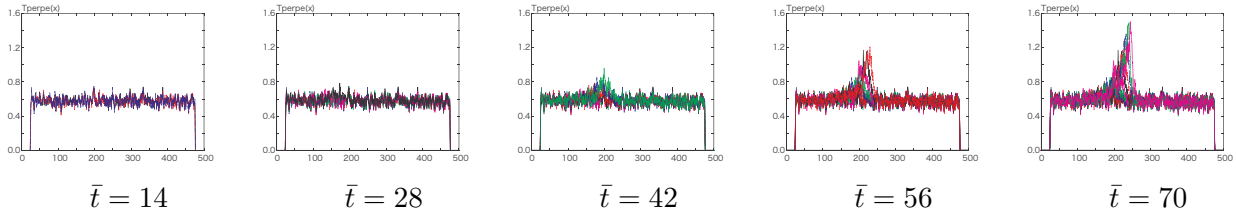

Fig 4: Electron temperature averaged over y : heating by cyclotron resonance is observed

In order to reduce the discrete noise due to electromagnetic fluctuation, it is necessary to increase the number of particles per cell. Furthremore, to carry out the analytis with higher resolution, larger scale of calculation is needed. Therefore we have implumented high speed cauculation by parallelization, MPI and OpenMP. Using computer cluster with 8 nodes and 64 cores, computation time with number of proceeses n_{pr} in MPI, and number of threads n_{th} in OpenMP are shown in Table 1. Computation time without any parallelization is $360s$, while parallel calculation 14 times higher than the case without parallelization is realized. Parallel number with 2 process and 4 threads per node provides best perforance. Computation times as a function of the node number is shown in Table 2. It is confirmed that with the increase of the number of nodes, the computation time is monotonically reduced.

n_{th} \ n_{pr}	1	2	4	8
1	52 s	33 s	28 s	41 s
2	33 s	26 s	27 s	36 s
4	26 s	25 s	35 s	49 s
8	26 s	34 s	46 s	77 s

Table 1: Computation time as a function of the number of processes n_{pr} and the number of threads n_{th} on one node

the number of node	1	2	4	8
computation times	84 s	50 s	33 s	25 s

Table 2: Computation time as a function of the number of nodes with 2 processes and 4 threads per node

4 Remaining issues

The remaining issues include to develop physical model, like plasma production by ionization, to confirm the conversion to the Berstein wave which requires large-scale computation, and to enhance computational performance, full-scale parallelization with and introdution of region splitting.

[1] H.Naitou, S,Satake, J. Plasma Fusion Res. Vol.89, No.4 (2013)245-260.

Start-up simulation of burning plasma by integrated modeling code TASK

Kazuki Nagai[1], Atsushi Fukuyama[1], Hideo Nuga[2]

[1]Graduate School of Engineering, Kyoto University
[2]National Institute for Fusion Science

The start up of burning plasma has to be carried out within a limited external heating power. Therefore, it is important to analyze the behavior of fast fuel ions quantitatively and self-consistently. To simulate the start up of ITER burning plasma, a tool to analyze the time evolution of momentum distribution functions of fuel ions has been developed by using the integrated code TASK for tokamak core plasmas.

1 Introduction

In order to describe the behavior of burning plasmas, it is required to calculate the enhancement of the fusion reaction rate by the fast fuel ions produced by neutral beam injection or ion-cyclotron wave heating. High resolution in momentum space is required for correctly analyzing the wide energy range from 1keV to 3.5MeV in the start-up phase. In order to improve the momentum resolution and the computational performance, TASK/FP[1] was parallelized with respect to the minor radius, the momentum and the particle species.

The purpose of this study is to simulate ITER burning plasma start-up including time evolution of momentum distribution functions of fuel ions by the use of the integrated code TASK for tokamak core plasma.

2 Numerical model

The TASK/FP describes the time evolution of momentum distribution functions $f_s(p, \theta, \rho, t)$ for particle specie s by solving the bounce averaged drift kinetic equation of the Fokker-Planck type

$$\frac{\partial f_s}{\partial t} = E(f_s) + C(f_s) + Q(f_s) + D(f_s) + S_s, \tag{1}$$

where p is the magnitude of momentum, θ the pitch angle, ρ the normalized minor radius, $E(f_s)$ acceleration term by DC electric field, $C(f_s)$ non-Maxwellian Coulomb collision term, $Q(f_s)$ quasi-linear diffusion term due to interaction with waves, $D(f_s)$ radial diffusion term, and S_s source and sink term (NBI and fusion reaction).

In calculating the Coulomb collision term, the background particle is assumed to be Maxwellian velocity distribution in conventional Fokker-Planck analysis. In the present analysis, the background particle specie is a non-Maxwellian velocity distribution, the solution of equation (1); therefore this model can describe the collisional effect correctly.

The radial diffusion term affects the radial transport of particles and heat. Two transport models are used. One is the model which assumes that the radial diffusion coefficients are parabolic in space and fixed value in time, and the other is the CDBM turbulent transport

model[2] which is considered to be more realistic and depends on plasma density and temperature gradient. Since fast ions which have a large cyclotron radius feel spatially averaged turbulence fluctuation, the radial diffusion constant is assumed to be inversely proportional to the magnitude of momentum. In addition we have reproduced H-mode transport behavior by reducing the diffusion constant in edge region $\rho \geq 0.85$.

3 Numerical results

We consider a tokamak plasma which consists of electron, deuterium ion, tritium ion, and α particle (helium ion). We assume initial temperature of 2.5 keV, and heating by the deuteron NBI 50 MW. The fuel ion (deuterium and tritium) is continuously injected into the plasma simulating intermittent pellet injection. Changing the collision model (background Maxwellian distribution or non-Maxwellian distribution) and the radial diffusion model, the simulation was performed in order to look for the operation scenario in which a steady state $Q = 10$ is maintained where Q is the power multiplication factor.

Figure 1 shows the 30 seconds time evolution of the power multiple factor for two collision models. Since the background Maxwellian distribution model assumes that the background particles have a Maxwellian momentum distribution using the temperature evaluated by the average kinetic energy which is higher than the bulk temperature, the tritium ions are mainly heated by collision with NBI ion. Since the existence of fast particles is considered accurately in the non-Maxwellian distribution model, however the electrons are heated at the beginning. The large difference of the power multiplication factor is attributed to the initial collisional heating.

Figure 2 shows the momentum distribution function of the deuterium ion for every 5 sec. While the NBI peak can be seen in $t = 6$ sec and $t = 9$ sec immediately after heating start, it is difficult to observe at $t = 15$ sec because α particle heating dominates. Figure 3 shows the time evolution of volume averaged density and temperature for the deuterium ion. Figures 4 and 5 show the radial profiles of the density and temperature of the deuterium ion for every 1 second.

The volume averaged density saturates, while the temperature increases exponentially. and the steady state cannot be achieved with constant heating power due to thermal runaway. Therefore it is conclude that it is necessary to optimize and control heating power and fuel supply using pellets in order to realize steady state.

4 Remaining issues

The remaining issues are simultaneous heating simulation of core plasma including IC heating and EC heating as well as NBI heating, maintaining steady state by controlling heating power and fuel injection[3], and comparison with the analysis using 1D diffusive transport code TASK/TR.

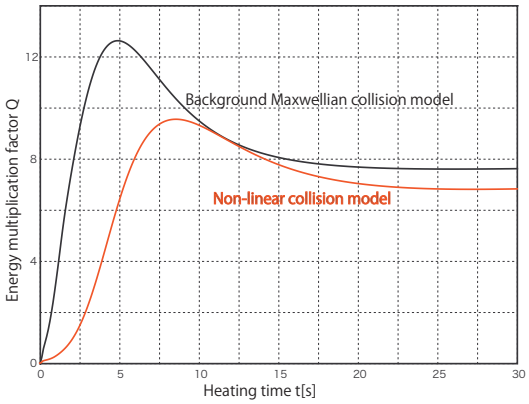

Fig.1.Time evolution of energy multiple

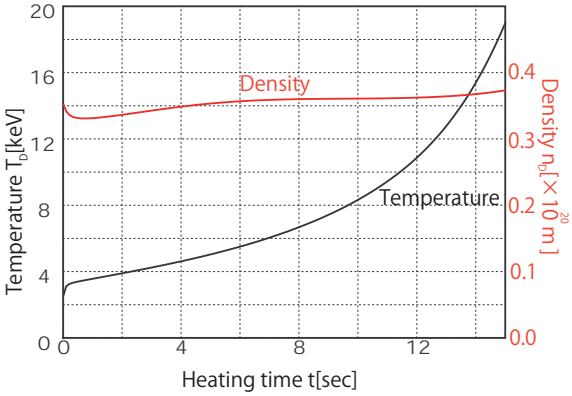

Fig.3.Time evolution of density and temperature

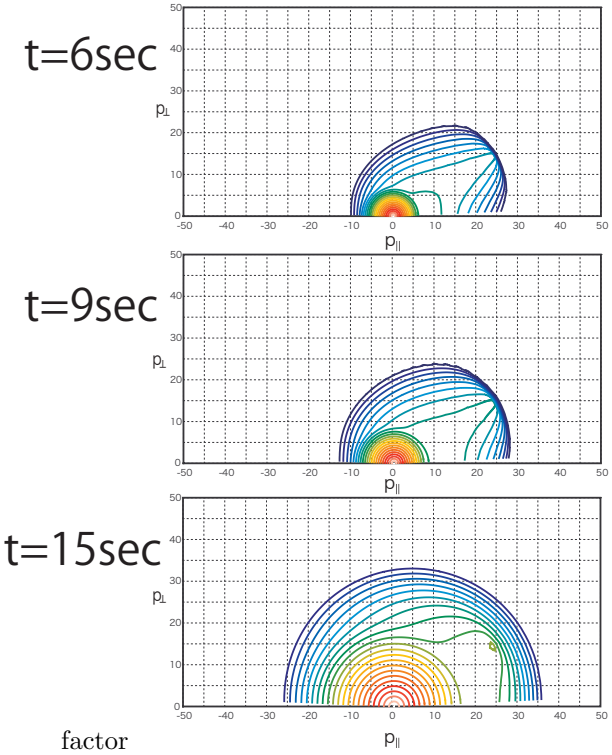

factor

Fig.2.Momentum distribution function

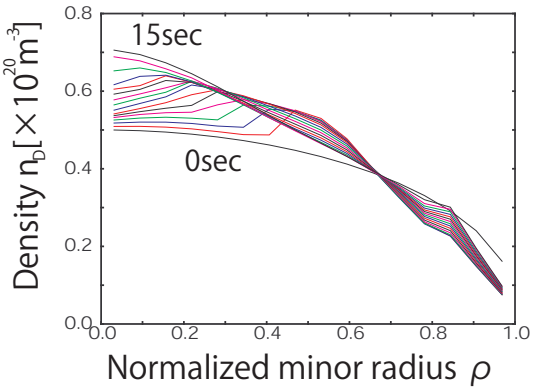

Fig.4.Radial density profile

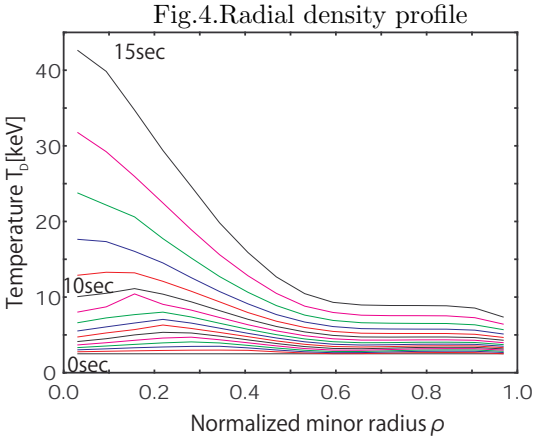

Fig.5.Radial temperature profile

References

[1] H. Nuga, A. Fukuyama, Progress in nuclear science and technology. Volume **2**, pp78-84 (2011)

[2] A. Fukuyama, K. Itoh, S-I. Itoh, M.Yagi, M. Azumi, Plasma Phys. Control. Fusion Volume **37** 611-631 (1995)

[3] Y. Miyoshi, Y. Ogawa, Plasma and Fusion Res. Volume **9**, 1405015 (2014)

Construction of reduced transport model by gyro-kinetic simulation with kinetic electrons in helical plasmas

S. Toda, M. Nakata, M. Nunami, A. Ishizawa[1], T. -H. Watanabe[2] and H. Sugama
National Institute for Fusion Science, Oroshi-cho 322-6, Toki, Gifu, 509-5292, Japan
[1]*Graduate School of Energy Science, Kyoto Uni., Gokasho, Uji, Kyoto, 611-0011, Japan*
[2]*Department of Physics, Nagoya University, Furo-cho, Nagoya, Aichi, 464-8602, Japan*

Turbulent transport is one of the most critical issues for plasma confinement in magnetic fusion devices. This is because the turbulent transport induces a large amount of the particle and heat loss in toroidal plasmas. The optimization by improving the turbulent transport due to the plasma micro-instabilities is expected. Recently, a large number of the gyro-kinetic simulations which is applied to the turbulent transport have been done in toroidal plasmas. The gyro-kinetic simulation results in tokamak and helical plasmas have been studied with the experimental observations. It is well-known that helical systems have the advantage in maintaining a steady state for the long plasma discharge. Gyro-kinetic simulations of helical plasmas need a large number of mesh points along the field line to catch the helical ripple structure.

The GKV-X code [1] solving the gyro-kinetic equation has been used to examine the ion temperature gradient (ITG) mode and zonal flows in the Large Helical Device (LHD) for studying the turbulent transport in helical plasmas [2]. The gyro-kinetic simulation with the adiabatic electron is performed for the high ion temperature LHD discharge (shot number 88343 [3]). This reduced model for the ion heat diffusivity is proposed [4] using the GKV-X code for the transport simulation. The reduced model is the function of the linear growth rate for the ITG mode and the zonal flow decay time [5, 6]. It is costly to carry out linear calculations of the growth rate by the gyro-kinetic simulation at each time step of the dynamical transport code such as TASK3D [7], because the transport analysis of helical plasmas demands a high radial resolution so as to accurately evaluate the radial electric field and the field configuration. In tokamak plasmas, the gyro-kinetic simulations at each time step are globally done in the dynamical transport simulation. How to apply the reduced model of the turbulent heat diffusivity for the ITG mode derived from the gyro-kinetic simulation to the transport code has been shown in helical plasmas with a low computational cost [8]. The calculation by substituting the the linear growth rate integrated over the poloidal wavenumber space and the zonal flow decay time to the reduced model [4] reproduces the results of the reduced model itself within allowable errors. The ion heat flux by the ITG mode instability agrees with the experimental results [2, 4]. The transport simulation results using the adiabatic electron for the T_i profile do not contradict with the experimental observation [8]. However, the gyro-kinetic simulation with the kinetic electrons shows the larger ion heat flux than the experimental results in the LHD [9]. The value of the electron energy flux by the gyro-kinetic simulation with the kinetic electrons is close to that in the experimental results of the LHD [9]. The effect of the kinetic electrons induces the enhancement of the linear growth rate of ITG modes. On the other hand, the effect of the finite β reduces the linear growth rate of the ITG modes. To compare the gyro-kinetic simulation results with the experimental results with respect to the turbulent ion heat diffusivity, these effect of the kinetic electrons and the finite β on the plasma instability should be included.

In order to examine the effect of the kinetic electrons, the reduced model of the ion heat diffusivity for the ITG mode is needed to be constructed by solving the gyro-kinetic equation in terms of the electron in addition to the ion. The finite β effect is included in the gyro-kinetic simulation. The plasma parameter region of the poloidal wavenumber is studied $0.1 \leq \tilde{k}_y \leq 0.5$, where the ITG

mode becomes unstable, where $\tilde{k_y} = k_y \rho_i$. The same method with the gyro-kinetic analysis using the adiabatic electrons [4] is adapted to construct the reduced model of the ion heat diffusivity as the function of the linear growth rate and the characteristic quantity of zonal flows. The nonlinear gyro-kinetic simulation with the kinetic electrons is performed to derive the value of the ion heat diffusivity.

We examined the turbulence driven by the microinstabilities in LHD plasmas by using the gyro-kinetic local flux tube code GKV-X [1]. The gyro-kinetic equation for non adiabatic part is solved in the flux tube coordinate (x, y, z), where $x = a(\rho - \rho_0)$, $y = a\rho_0(q(\rho) - \zeta)/q_0$ and $z = \theta$ with the flux coordinate (ρ, θ, ζ). Here, q_0 is the safety factor at the flux surface of ρ_0 and a is the minor radius. The density, the electron and the ion temperatures at $t = 2.233$s in the high-T_i discharge #88343 [3] are used. The GKV-X simulation with the kinetic electrons is performed for the three dimensional equilibrium field configuration with $R = 3.75$m, using the plasma profiles in the VMEC calculation. The finite β effect is included, where $\beta = 0.3\%$ at $\rho = 0.65$, for example. To reduce computer resources and perform the nonlinear GKV-X simulation in the wider plasma parameter region, we take smaller Fourier modes and the smaller number of the grid points in this simulation than the case in [9]. The total Fourier mode numbers in the x and y direction are 16 and 16. The total Fourier mode numbers in the $\tilde{k}_x$ and $\tilde{k}_y$ direction are 8 and 6 in the region $-0.5 \leq \tilde{k}_x \leq 0.5$ and $0.0 \leq \tilde{k}_y \leq 0.5$, where $\tilde{k}_x (= k_x \rho_i)$ is the normalized radial wavenumber. The total grid number in the parallel direction, the parallel velocity direction and the perpendicular velocity direction are 256, 64 and 16, respectively. We carry out nonlinear GKV-X nonlinear simulations at ten radial points between $\rho = 0.46$ and $\rho = 0.80$. The time evolution of the total ion energy flux Q_i at $\rho (= r/a) = 0.65$ is examined as the results of the gyro-kinetic simulation with the kinetic electrons. The value of time t is normalized by R/v_{ti}, where R is the major radius and v_{ti} is the ion thermal velocity, $\sqrt{T_i/m_i}$. The saturation of the ion energy flux is obtained in the nonlinear phase. The averaged value of the ion energy flux in the time interval $50 < t < 100$ is 0.12 MW/m^2. In ref. [9], the averaged value of the ion energy flux in the time interval $50 < t < 80$ is about 0.13 MW/m^2, when the Fourier mode numbers in the $\tilde{k_x}$ and $\tilde{k_y}$ direction are 256 and 43. Even if the number of the Fourier modes is only 8 and 6 in the $\tilde{k}_x$ and $\tilde{k}_y$ directions, respectively, the close value of the ion energy flux can be obtained in this study. The time evolution of the ratio of the electromagnetic contribution Q_i^{em} to the total ion heat flux Q_i is also studied. The averaged value of $|Q_i^{em}|/Q_i$ in the time interval $50 < t < 100$ is 0.33%, because of the low beta 3% plasma. The saturation of the electron heat flux is seen and the averaged value of the ion energy flux in the time interval $50 < t < 100$ is 0.070 MW/m^2. The averaged value of the electron heat flux in the interval $50 < t < 80$ is about 0.058 MW/m^2. However, the time averaged value in the time window $50 < t < 100$ of the ratio of the electromagnetic contribution to the total electron heat flux becomes about 30%, even if the low beta 3% plasma. If the larger number of the modes is taken, the electromagnetic part becomes much smaller [9]. Therefore, we focus on the construction of the reduced model for the ion heat diffusivity in this article. The time evolutions of the squared turbulent potential fluctuation, $\mathcal{T}\left(= \Sigma_{k_x, k_y \neq 0} \left\langle \left| \tilde{\phi}_{k_x, k_y} \right|^2 \right\rangle /2\right)$ and the squared zonal flow potential, $\mathcal{Z}\left(= \Sigma_{k_x} \left\langle \left| \tilde{\phi}_{k_x, k_y = 0} \right|^2 \right\rangle\right)/2$ are obtained, where $\tilde{\phi}$ is the normalized electrostatic potential fluctuation which is defined as $\tilde{\phi} = \phi/(T_i \rho_i/(eR))$. Here, the bracket $\langle\rangle$ represents the averaged values along the magnetic field line. The nonlinear saturation is shown in the time evolution of $\mathcal{T}$ and $\mathcal{Z}$.

Based on the temperatures and density radial profiles and field configuration from the LHD experimental results of high-T_i phase at $t = 2.233$s, the electron and ion temperature gradients, R/L_{T_e}

and R/L_{T_i}, the normalized density gradient R/L_n and the safety factor q radially change. The radial profiles of the ion heat diffusivity $\bar{\chi}_i$ are compared by the gyro-kinetic nonlinear simulation with the kinetic electrons and the adiabatic electrons. Here, the bar $^-$ shows the averaged value in the time interval $50 < t < 100$ of the nonlinear saturation phase. The values of $\bar{\chi}_i$ by the simulation with the kinetic electrons are from two to three times larger than those by the simulation with the adiabatic electrons. The normalized electron and ion temperature gradients are artificially altered from 0.8 to 1.2 times the experimental values at $\rho = 0.46$, $\rho = 0.50$, $\rho = 0.54$, $\rho = 0.58$, $\rho = 0.62$, $\rho = 0.65$, $\rho = 0.68$, $\rho = 0.72$, $\rho = 0.76$ and $\rho = 0.80$. The transport coefficients $\bar{\chi}_i/\chi_i^{GB}$ are compared with a model function of $\bar{\mathcal{T}}$ and $\bar{\mathcal{Z}}$ in figure 1. A fitting function [4] for the ion heat diffusivity is defined by

$$\frac{\bar{\chi}_i}{\chi_i^{GB}} = \mathcal{F}(\bar{\mathcal{T}}, \bar{\mathcal{Z}}) \equiv \frac{C_1 \bar{\mathcal{T}}^{\alpha}}{C_2 + \bar{\mathcal{Z}}^{\frac{1}{2}}/\bar{\mathcal{T}}}, \tag{1}$$

with $\alpha = 0.24$, $C_1 = 0.11$ and $C_2 = 1.8 \times 10^{-3}$, where χ_i^{GB} is the gyro-Bohm diffusivity. The relative error for fitting $\bar{\chi}_i/\chi_i^{GB}$ by $\mathcal{F}$ is 0.31, in spite of the wide parameter range in the nonlinear simulation, where the relative error is defined as the root mean square of $\left[(\bar{\chi}_i/\chi_i^{GB})/\mathcal{F} - 1\right]$. Therefore, the value of the ion heat diffusivity is well reproduced by the model function eq. (1).

The gyrokinetic simulation with the kinetic electrons is performed to construct the transport model for the turbulent ion heat diffusivity. The values of the ion heat diffusivity are derived from the nonlinear gyro-kinetic simulation for high-T_i mode in the LHD, where the ITG mode is destabilized. The nonlinear simulation results for the ion heat diffusivity with the kinetic electrons are compared with those by the simulation with the adiabatic electrons. The model function for the ion heat diffusivity is shown in terms of the squared turbulent electrostatic potential fluctuation and the squared zonal flow potential. The reduced model for the ion heat diffusivity will be constructed by the electromagnetic gyro-kinetic simulation with kinetic electrons. The reduced transport models for the electron heat diffusivity and the particle diffusivity in addition to ion heat diffusivity will be studied when the total Fourier mode number increases. These is left for future study. This work was partly supported by JSPS KAKENHI Grant Number 23561002, the NIFS Collaboration Research program (Plasma Simulator), NIFS16KNST093 and the Collaborative Research Program of Research Institute for Applied Mechanics, Kyushu University.

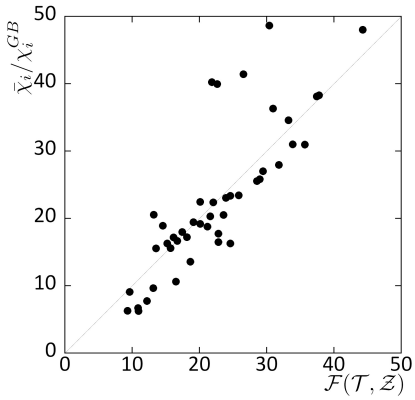

Figure 1: Comparison of $\bar{\chi}_i/\chi_{GB}$ from the nonlinear gyro-kinetic simulation with the model function $\mathcal{F}(\bar{\mathcal{T}}, \bar{\mathcal{Z}})$.

[1] T. -H. Watanabe and H. Sugama Nucl. Fusion **46** 24 (2006)
[2] M. Nunami, T. -H. Watanabe, H. Sugama and K. Tanaka, *Phys. Plasmas* **19** 042504 (2012)
[3] K. Tanaka, et al., *Plasma Fusion Res.* **5** S2053 (2010)
[4] M. Nunami, T. -H. Watanabe and H. Sugama, *Phys. Plasmas* **20** 092307 (2013)
[5] H. Sugama and T. -H. Watanabe, *Phys. Plasmas* **13** 012501 (2006)
[6] S. Ferrando-Margalet, H. Sugama and T. -H. Watanabe *Phys. Plasmas* **14** 122505 (2007)
[7] M. Yokoyama, et al., *Plasma Fusion Res.* **7** 2403011 (2012)
[8] S. Toda et al., *Journal of Physics: Conference Series* **561** 012020 (2014)
[9] A. Ishizawa et al., *Nucl. Fusion* **55** 043024 (2015)